Supporting information

Valence-Free Open Nanoparticle Superlattices

Binay P. Nayak,[†] Wenjie Wang,[‡] Prapti Kakkar,[†] Honghu Zhang,[¶] Zinnia Mallick,[§] Shan Zhou,[§] Dmytro Nykypanchuk,[‖] Surya K. Mallapragada,[†] Alex Travesset,[*,⊥] David Vaknin,[*,⊥]

†*Ames National Laboratory, and Department of Chemical and Biological Engineering, Iowa State University, Ames, IA 50011, USA*

‡*NSLS-II, Brookhaven National Laboratory, Upton, NY 11973, USA*

¶*Ames National Laboratory, and Department of Physics and Astronomy, Iowa State University, Ames, IA 50011, USA*

§ *Department of Nanoscience and Biomedical Engineering, South Dakota School of Mines and Technology, Rapid City, SD, 57701, USA*

‖ *Center for Functional Nanomaterials, Brookhaven National Laboratory, Upton, NY, 11973, USA*

⊥*Division of Materials Sciences and Engineering, Ames National Laboratory, Ames, IA 50011, USA*

∗ To whom correspondence should be addressed. E-mail: trvsst@ameslab.gov, vaknin@ameslab.gov

This PDF file includes the following information:

- Supplementary Text
- Figures S1-S35
- References 29-41

DLS and ζ potential characterizations

DLS Data Analysis to Determine Hydrodynamic Size

The hydrodynamic size distribution of PEG-coated AuNPs was analyzed using DLS. The raw DLS intensity curves were fitted to a log-normal function to extract the peak center and peak width, providing detailed insights into the size distribution. The log-normal fit equation used for the analysis is as follows:

$$f(x) = A \cdot \exp\left(-\frac{(\ln(x) - \text{cen})^2}{2 \cdot \text{wid}^2}\right) \tag{S1}$$

where A represents the amplitude of the distribution, cen is the logarithmic center (corresponding to the modal hydrodynamic size in the linear scale, i.e. exp(cen)), and wid is the logarithmic width describing the spread of the distribution.

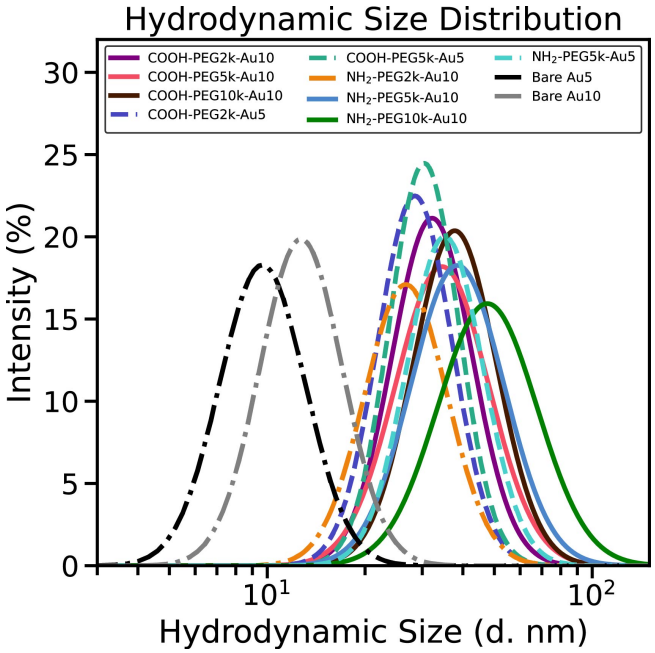

Fig. S1. DLS intensity percentage versus hydrodynamic size distribution for aqueous suspensions of bare AuNPs (dashed line) and PEG-grafted AuNPs (solid lines) at room temperature. The peak positions in the DLS measurements shift to larger hydrodynamic sizes as the MW of the PEG increases, indicating successful grafting of PEG to the AuNP surfaces. The modal D_H of each NP is summarized in Table S1.

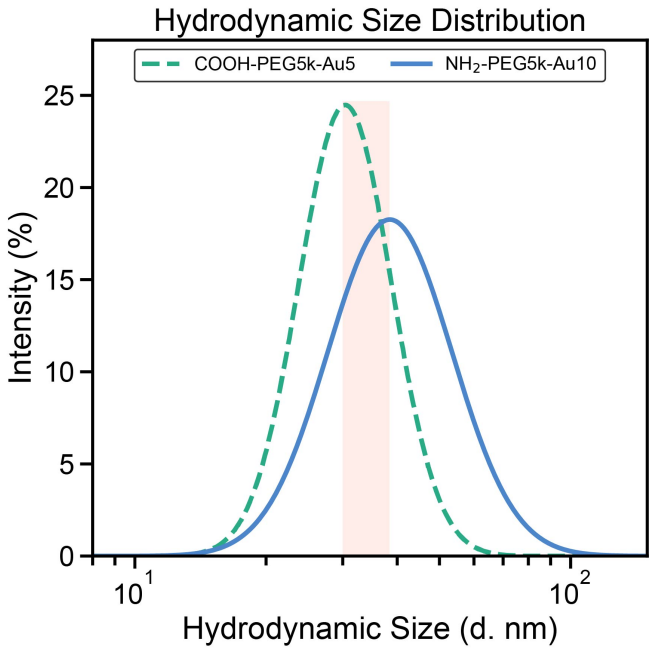

Fig. S2. DLS intensity distribution versus hydrodynamic diameter for aqueous suspensions of COOH-PEG5k-Au5 and NH_2-PEG5k-Au10 nanoparticles. The shaded region indicates the size range associated with the assembly of a CsCl-like superstructure (see Fig. S17). From this distribution, the effective size ratio, γ, is estimated to be 0.9 ± 0.1.

The modal hydrodynamic size was determined by extracting the peak center (cen) from the fitted curve and converting it to the linear scale (exp(cen)). The error bars for the size distribution were calculated using the logarithmic width (wid). Specifically, the width of the curve was scaled and propagated to estimate the uncertainty in the size measurements. This approach ensures that the error bars reflect the variability within the hydrodynamic size distribution. The hydrodynamic size parameters are listed in Table S1. All the γ values are calculated from values in Table S1; however, to create the CsCl structure and confirm the gamma corresponding to theory, the conditions are discussed below.

Fig. S2 shows the DLS intensity distribution for aqueous suspensions of COOH-PEG5k-Au5 and NH_2-PEG5k-Au10. It is used to demonstrate the concept of fractionalization (i.e., the spontaneous selection of a narrow size-distribution of particles to establish assembly into a specific superlattice) to rationalize the experimental results to conform with the phase diagrams. The distribution exhibits a distinct size range, highlighted by the shaded area, corresponding to the region where we

anticipate the assembly of a CsCl-like superstructure (refer to Fig. S17), possibly due to fractionalization. Analysis of the DLS data yields an effective size ratio, γ, of approximately 0.9 ± 0.1. Rather than using the numerically precise value $\gamma = 0.98$, we instead adopted $\gamma = 0.90$ to align with the DLS-derived hydrodynamic diameters, acknowledging the inherent experimental uncertainties. A small deviation in gamma doesn't affect the predicted lattice symmetry or stabilization. This measurement confirms that the particle sizes in our system are within the targeted range for CsCl superlattice formation, thereby consistent with the structural predictions.

Fig. S3 presents the DLS measurements for our aqueous suspensions of COOH-PEG10k-Au10 and NH_2-PEG5k-Au10 nanoparticles across a range of pH values. The DLS intensity distribution, plotted as a function of the hydrodynamic diameter, reveals that the D_H of the nanoparticles remains roughly consistent regardless of pH. This is evidenced by the stable peak positions and the minimal variation in the peak widths. These findings indicate that the nanoparticle-ligand assemblies are robust under the experimental conditions used, with negligible aggregation or degradation. This stability is critical for ensuring γ values presented in the main text.

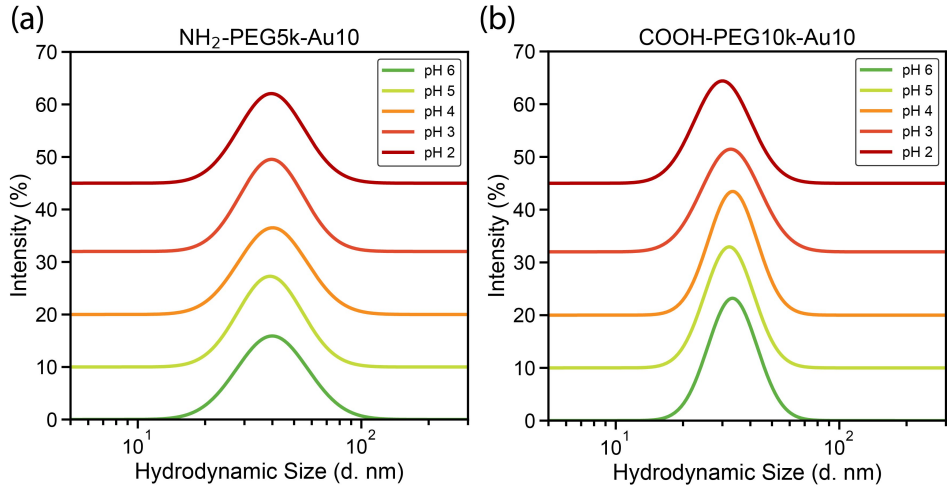

Fig. S3. Dynamic light scattering (DLS) intensity distribution versus hydrodynamic diameter for aqueous suspensions of COOH-PEG10k-Au10 and NH_2-PEG5k-Au10 measured at various pH values. The data confirm that the hydrodynamic diameter, D_H, remains essentially constant across the pH range, with only minimal changes in the peak width, indicating negligible variation in the size distribution.

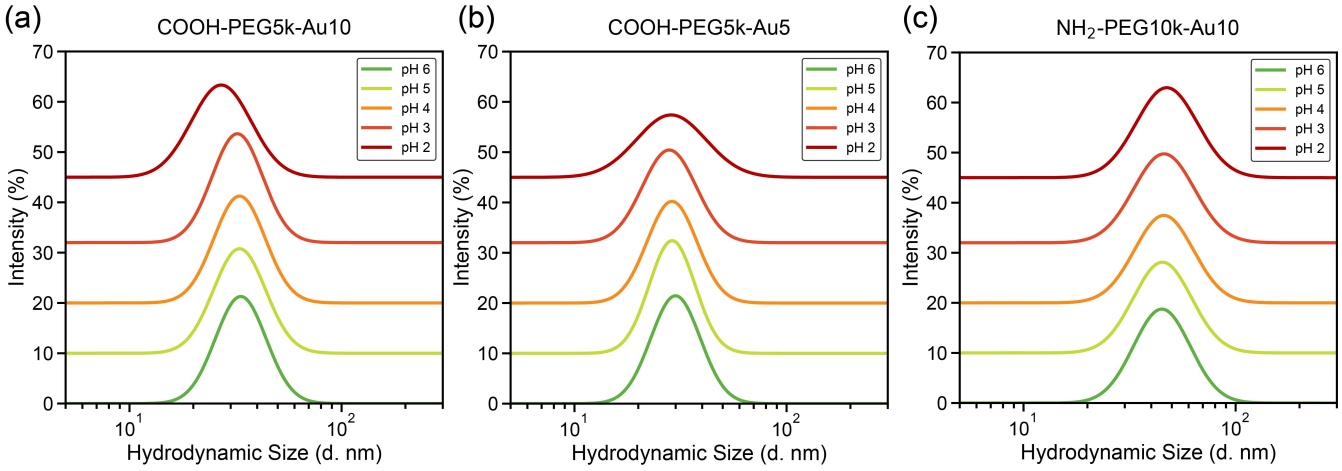

Fig. S4. Dynamic light scattering (DLS) intensity distribution versus hydrodynamic diameter for aqueous suspensions of COOH-PEG5k-Au10, COOH-PEG5k-Au5 and NH_2-PEG10k-Au10 measured at various pH values. The data confirm that the hydrodynamic diameter, D_H, remains essentially constant across the pH range, with only minimal changes in the peak width, indicating negligible variation in the size distribution.

Table S1: Modal hydrodynamic size and $\zeta-$potential values of AuNPs Samples in water

AuNP Size[1](nm)	End Group of Grafted PEG	PEG MW (kDa)	Nomenclature	Hydrodynamic Size[3](nm)	$\zeta-$potential[4] (mV)
Au10	COOH	2	COOH-PEG2k-Au10	32.2 ± 1.3	-34.2 ± 3.4
		5	COOH-PEG5k-Au10	34.5 ± 1.4	-33.0 ± 2.5
		10	COOH-PEG10k-Au10	37.8 ± 1.3	-31.4 ± 3.1
	NH_2	2	NH_2-PEG2k-Au10	29.7 ± 1.3	$+8.3 \pm 3.6$
		5	NH_2-PEG5k-Au10	38.5 ± 1.4	$+11.1 \pm 2.6$
		10	NH_2-PEG10k-Au10	49.6 ± 1.4	$+14.3 \pm 3.9$
	Bare[2]	$--$	$----$	12.7 ± 0.7	-40.5 ± 1.9
Au5	COOH	2	COOH-PEG2k-Au5	28.5 ± 1.3	-34.8 ± 2.1
		5	COOH-PEG5k-Au5	30.4 ± 1.3	-26.3 ± 3.8
	NH_2	5	NH_2-PEG5k-Au5	35.2 ± 1.3	$+4.4 \pm 1.1$
	Bare[2]	$--$	$----$	9.7 ± 0.7	-30.4 ± 3.9

[1] The diameter is provided by the vendor. [2] The bare-surface AuNPs are stabilized by citrate ligands. [3] Only the modal size from the distribution profile is reported. [4] Only the modal $\zeta-$potential from the distribution profile is reported.

TEM Size Ditribution

Bright-field TEM imaging was used to compare particle size provided by the vendor shown in Fig. S5 for 5 nm and Fig. S6 for 10 nm AuNPs with their respective gaussian size distribution.

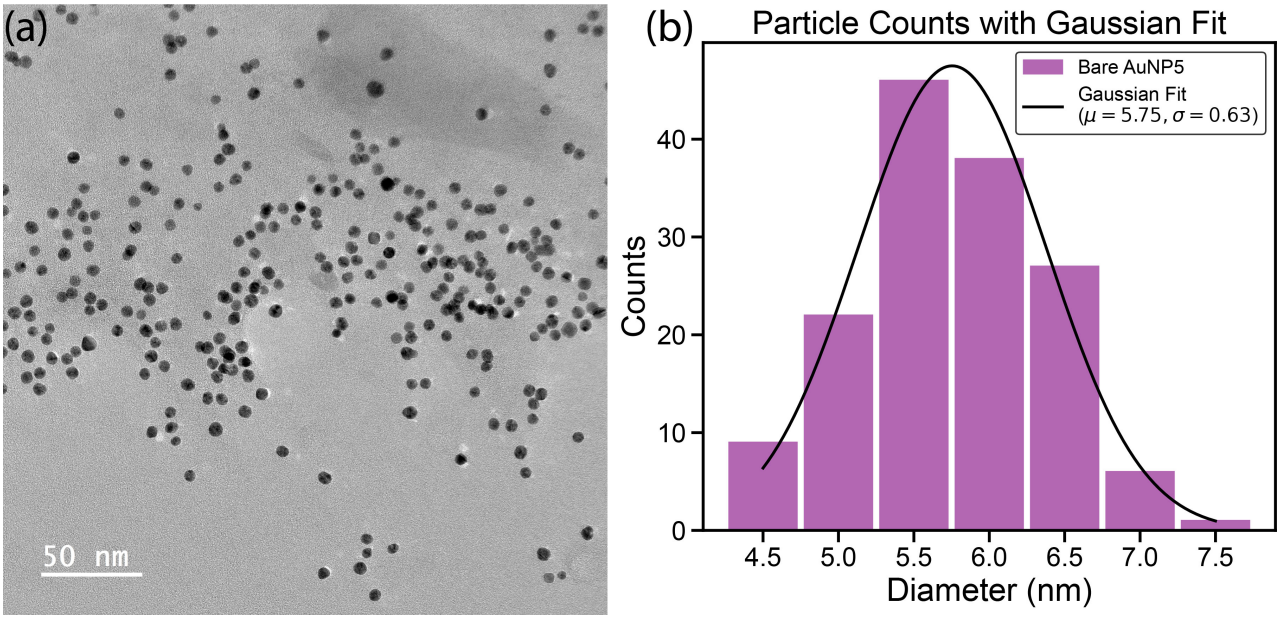

Fig. S5. (a) Bright-field TEM image of citrate-capped bare AuNP5 with a scale bar of 50 nm. (b) Histogram illustrating the particle size distribution of the AgNPs from image (a), overlaid with a Gaussian fit. The Gaussian fit indicates a mean particle size of 5.75 ± 0.63 nm.

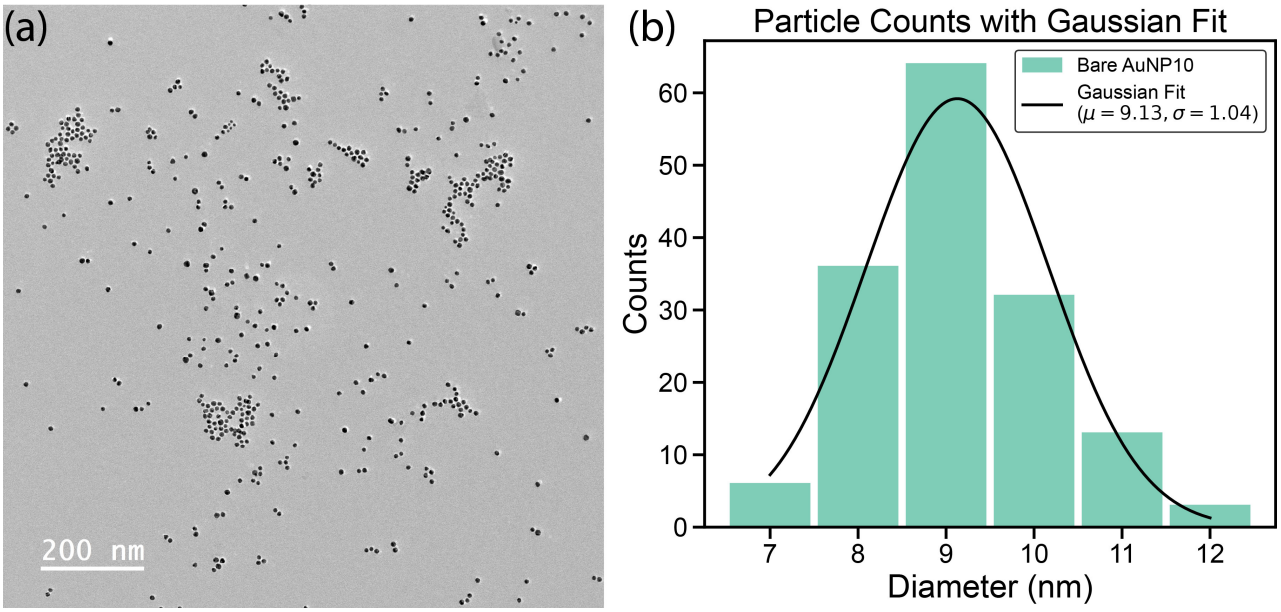

Fig. S6. (a) Bright-field TEM image of citrate-capped bare AuNP5 with a scale bar of 200 nm. (b) Histogram illustrating the particle size distribution of the AgNPs from image (a), overlaid with a Gaussian fit. The Gaussian fit indicates a mean particle size of 9.13 ± 1.04 nm.

Additional SAXS data

Figs. S9–S20 present systematic SAXS diffraction patterns acquired under various pH conditions and particle number ratios. Each figure includes detailed information on the experimental parameters (γ and θ), as well as the measured lattice constants, A-A nanoparticle, and A-B nanoparticle nearest-neighbor distances.

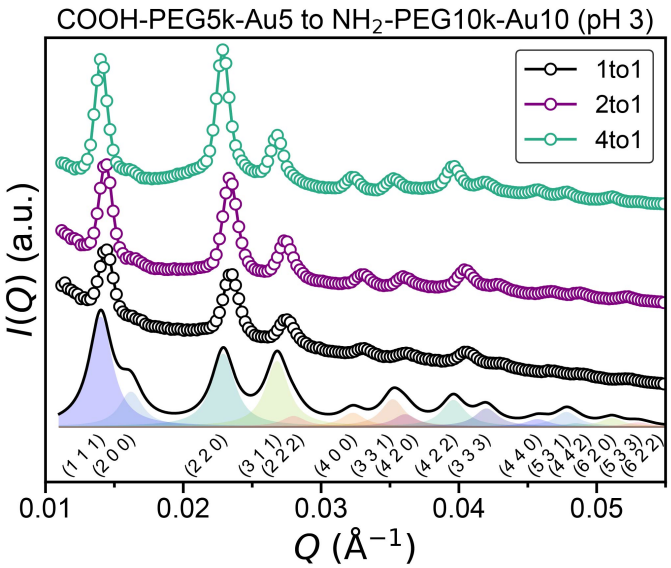

Component A	Component B	γ	θ
COOH-PEG5k-Au5	NH_2-PEG10k-Au10	0.60	0.5

Mixing Ratio (A:B)	1to1	2to1	4to1
Lattice Type	ZnS-like	ZnS-like	ZnS-like
Lattice Constant (a_L)	~ 76 nm	~ 76 nm	~ 78 nm
A-A Nearest Neighbor (d_{NN})	~ 54 nm	~ 54 nm	~ 55 nm
A-B Nearest Neighbor (d_{NN})	~ 33 nm	~ 34 nm	~ 34 nm

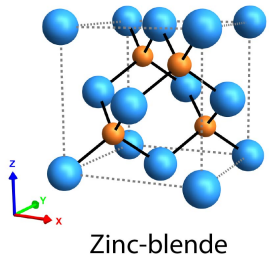

Fig. S7. SAXS diffraction patterns ($I(Q)$ vs. Q) for binary mixtures of COOH-PEG5k-Au5 and NH_2-PEG10k-Au10 at various mixing ratios, as indicated, at pH 3. The modeled intensity profiles corresponding to a zinc-blende lattice are shown as solid black lines, with individual peak contributions shaded below. The diffraction patterns for all three mixing ratios closely match the calculated diffraction pattern for a zinc-blende lattice. Relevant lattice parameters for each structure are summarized in the table adjacent to the plot, with a schematic representation of the zinc-blende lattice provided below the table for reference.

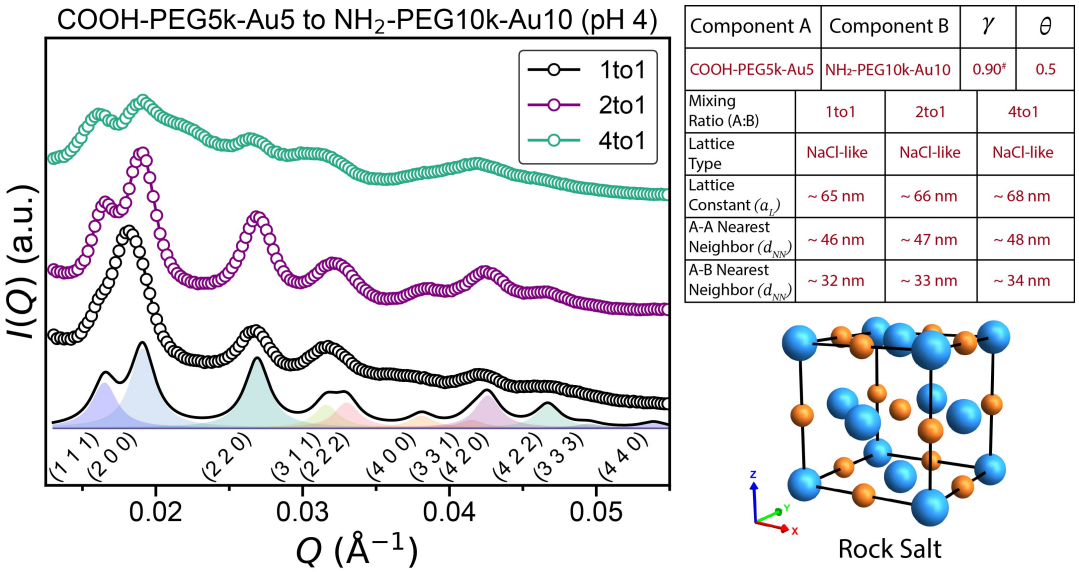

Component A	Component B	γ	θ
COOH-PEG5k-Au5	NH_2-PEG10k-Au10	0.90*	0.5

Mixing Ratio (A:B)	1to1	2to1	4to1
Lattice Type	NaCl-like	NaCl-like	NaCl-like
Lattice Constant (a_L)	~ 65 nm	~ 66 nm	~ 68 nm
A-A Nearest Neighbor (d_{NN})	~ 46 nm	~ 47 nm	~ 48 nm
A-B Nearest Neighbor (d_{NN})	~ 32 nm	~ 33 nm	~ 34 nm

Fig. S8. SAXS diffraction patterns ($I(Q)$ vs. Q) for binary mixtures of COOH-PEG5k-Au5 and NH_2-PEG10k-Au10 at various mixing ratios, as indicated, at pH 4. The modeled intensity profiles for the 1:1 and 2:1 mixtures correspond to a rock-salt lattice, shown as solid black lines, with individual peak contributions shaded below. The diffraction pattern of the 4:1 mixture reveals a meso-range order that departs from the long-range periodicity of the rock-salt–type superlattice; in particular, the broad shoulder on the (200) reflection points to defects, or even a short-range ordered phase, originating from the excess of smaller NPs in the bulk. Relevant lattice parameters for each structure are summarized in the table adjacent to the plot, with a schematic representation of the rock-salt lattice provided below the table for reference. $*$ represents the γ value estimated from NN distance.

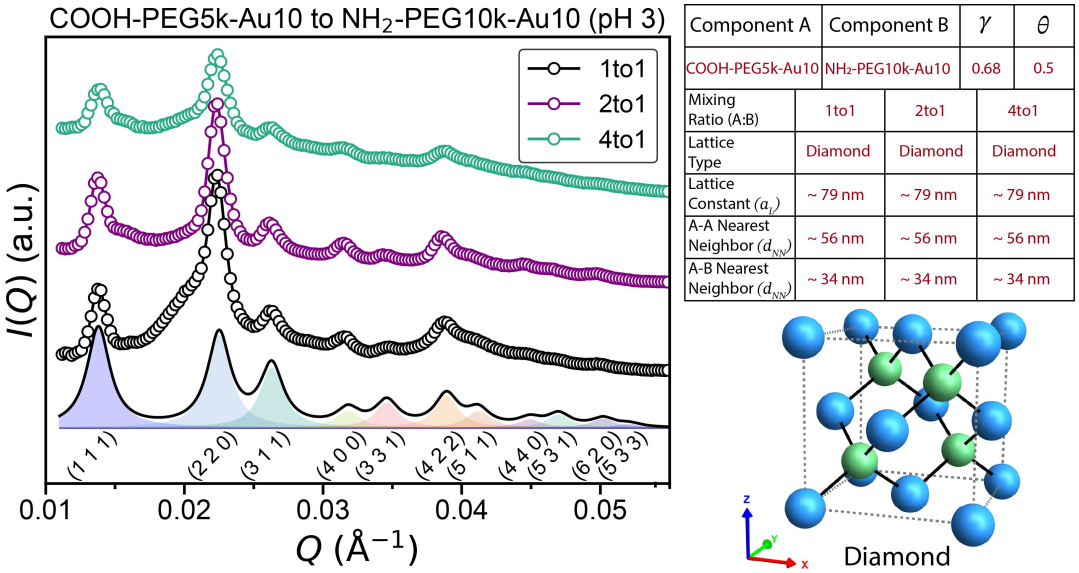

Component A	Component B	γ	θ
COOH-PEG5k-Au10	NH_2-PEG10k-Au10	0.68	0.5

Mixing Ratio (A:B)	1to1	2to1	4to1
Lattice Type	Diamond	Diamond	Diamond
Lattice Constant (a_L)	~ 79 nm	~ 79 nm	~ 79 nm
A-A Nearest Neighbor (d_{NN})	~ 56 nm	~ 56 nm	~ 56 nm
A-B Nearest Neighbor (d_{NN})	~ 34 nm	~ 34 nm	~ 34 nm

Fig. S9. SAXS diffraction patterns ($I(Q)$ vs. Q) for binary mixtures of COOH-PEG5k-Au10 and NH_2-PEG10k-Au10 at various mixing ratios, as indicated, at pH 3. The modeled intensity profiles corresponding to a diamond lattice are shown as solid black lines, with individual peak contributions shaded below. The diffraction patterns for all three mixing ratios closely match the calculated diffraction pattern for a diamond lattice. The black curve shows a weak, broad satellite shoulder on the (220) peak, consistent with defect formation or lattice elongation within an otherwise diamond-type lattice. Relevant lattice parameters for each structure are summarized in the table adjacent to the plot, with a schematic representation of the diamond lattice provided below the table for reference.

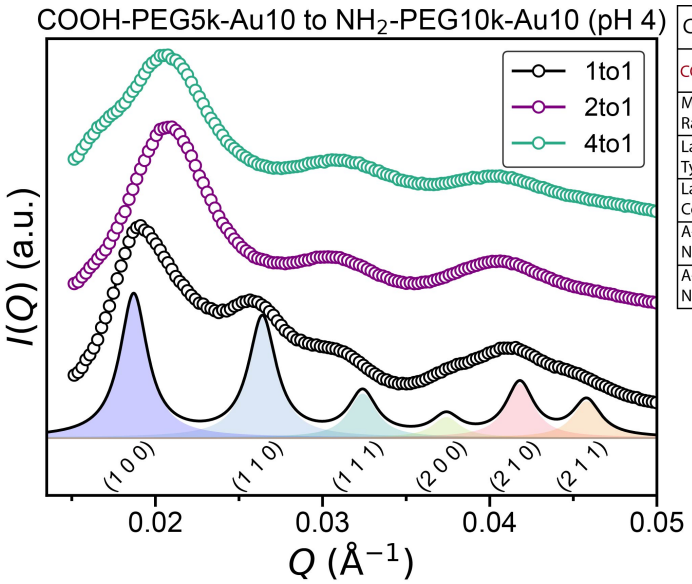

Component A	Component B	γ	θ
COOH-PEG5k-Au10	NH_2-PEG10k-Au10	0.96#	0.5

Mixing Ratio (A:B)	1to1	2to1	4to1
Lattice Type	Simple Cubic	SRO	SRO
Lattice Constant (a_L)	~ 33 nm	---	---
A-A Nearest Neighbor (d_{NN})	~ 47 nm	---	---
A-B Nearest Neighbor (d_{NN})	~ 33 nm	~ 30 nm	~ 30 nm

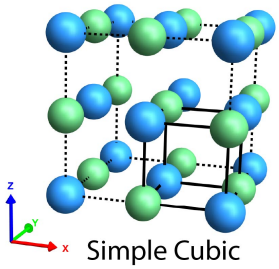

Fig. S10. SAXS diffraction patterns ($I(Q)$ vs. Q) for binary mixtures of COOH-PEG5k-Au10 and NH_2-PEG10k-Au10 at various mixing ratios, as indicated, at pH 4. The modeled intensity profiles for the 1:1 mixture correspond to a simple cubic lattice, shown as solid black lines, with individual peak contributions shaded below. The diffraction patterns for the other two mixing ratios (2:1 and 4:1) indicate cubic-like short-range motifs, which deviate from the long-range order of the simple cubic structure. Relevant lattice parameters for each structure are summarized in the table adjacent to the plot, with a schematic representation of the simple cubic lattice provided below the table for reference. # represents the γ value estimated from NN distance.

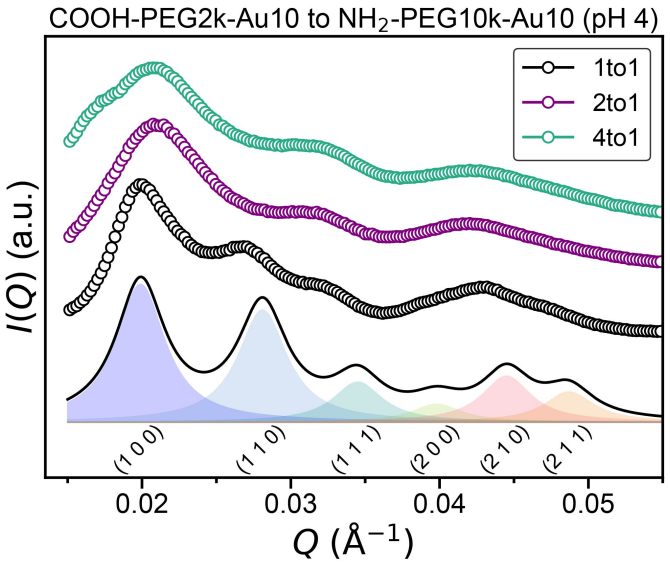

Component A	Component B	γ	θ
COOH-PEG2k-Au10	NH_2-PEG10k-Au10	0.90#	0.2

Mixing Ratio (A:B)	1to1	2to1	4to1
Lattice Type	Simple Cubic	SRO	SRO
Lattice Constant (a_L)	~ 32 nm	---	---
A-A Nearest Neighbor (d_{NN})	~ 45 nm	---	---
A-B Nearest Neighbor (d_{NN})	~ 32 nm	~ 30 nm	~ 30 nm

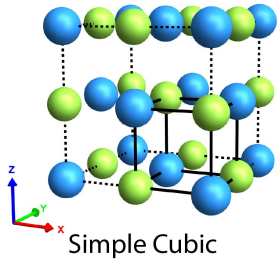

Fig. S11. SAXS diffraction patterns ($I(Q)$ vs. Q) for binary mixtures of COOH-PEG2k-Au10 and NH_2-PEG10k-Au10 at various mixing ratios, as indicated, at pH 4. The modeled intensity profiles for the 1:1 mixture correspond to a simple cubic lattice, shown as solid black lines, with individual peak contributions shaded below. The diffraction patterns for the other two mixing ratios (2:1 and 4:1) indicate cubic-like short-range motifs, which deviate from the long-range order of the simple cubic structure. Relevant lattice parameters for each structure are summarized in the table adjacent to the plot, with a schematic representation of the simple cubic lattice provided below the table for reference. # represents the γ value estimated from NN distance.

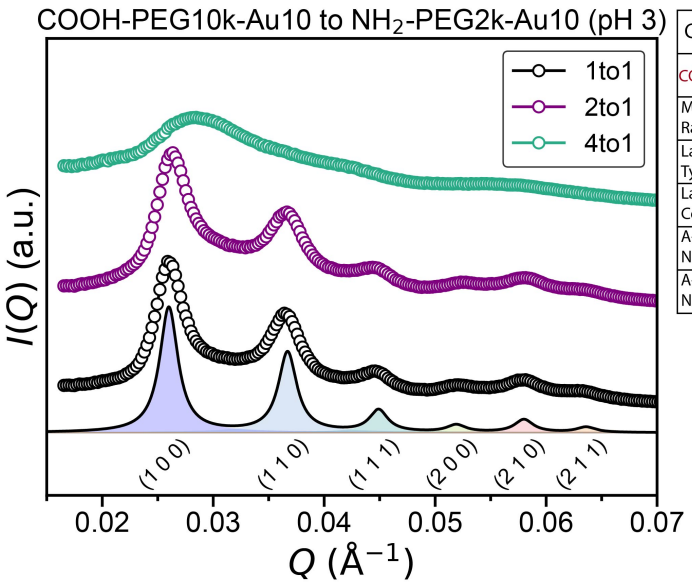

Component A	Component B	γ	θ
COOH-PEG10k-Au10	NH_2-PEG2k-Au10	0.80	5.0

Mixing Ratio (A:B)	1to1	2to1	4to1
Lattice Type	Simple Cubic	Simple Cubic	SRO
Lattice Constant (a_L)	~ 23 nm	~ 23 nm	---
A-A Nearest Neighbor (d_{NN})	~ 33 nm	~ 33 nm	---
A-B Nearest Neighbor (d_{NN})	~ 23 nm	~ 23 nm	~ 23 nm

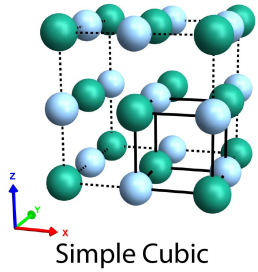

Fig. S12. SAXS diffraction patterns ($I(Q)$ vs. Q) for binary mixtures of COOH-PEG10k-Au10 and NH_2-PEG2k-Au10 at various mixing ratios, as indicated, at pH 3. The modeled intensity profiles for the 1:1 mixture correspond to a simple cubic lattice, shown as solid black lines, with individual peak contributions shaded below. The diffraction pattern for the 2:1 mixing ratio is similar to 1:1 and matches to cubic structure, while 4:1 shows broad humps indicative of SRO arrangements. Relevant lattice parameters for each structure are summarized in the table adjacent to the plot, with a schematic representation of the simple cubic lattice provided below the table for reference.

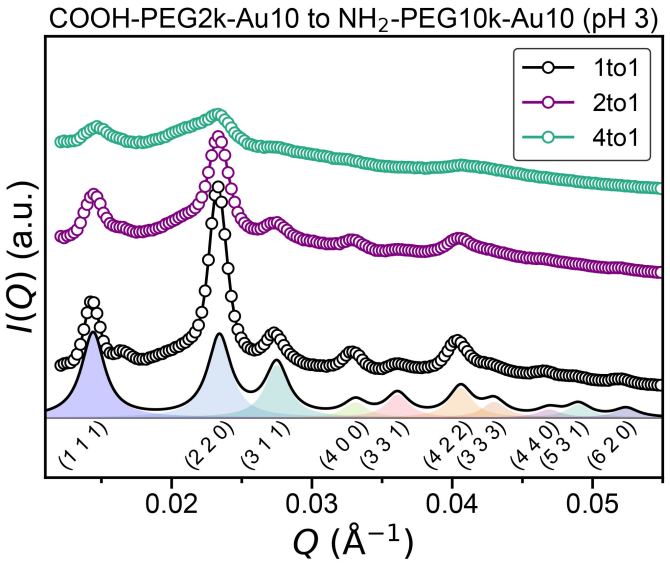

Component A	Component B	γ	θ
COOH-PEG2k-Au10	NH_2-PEG10k-Au10	0.64	0.2

Mixing Ratio (A:B)	1to1	2to1	4to1
Lattice Type	Diamond	Diamond	Diamond (MRO)
Lattice Constant (a_L)	~ 76 nm	~ 75 nm	~ 74 nm
A-A Nearest Neighbor (d_{NN})	~ 54 nm	~ 53 nm	~ 52 nm
A-B Nearest Neighbor (d_{NN})	~ 33 nm	~ 34 nm	~ 34 nm

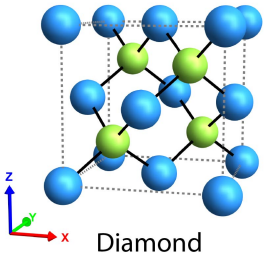

Fig. S13. SAXS diffraction patterns ($I(Q)$ vs. Q) for binary mixtures of COOH-PEG2k-Au10 and NH_2-PEG10k-Au10 at various mixing ratios, as indicated, at pH 3. The modeled intensity profiles corresponding to a diamond lattice are shown as solid black lines, with individual peak contributions shaded below. The diffraction patterns for all three mixing ratios closely match the calculated diffraction pattern for a diamond lattice, while the 4:1 mixture shows an MRO arrangement. Relevant lattice parameters for each structure are summarized in the table adjacent to the plot, with a schematic representation of the diamond lattice provided below the table for reference.

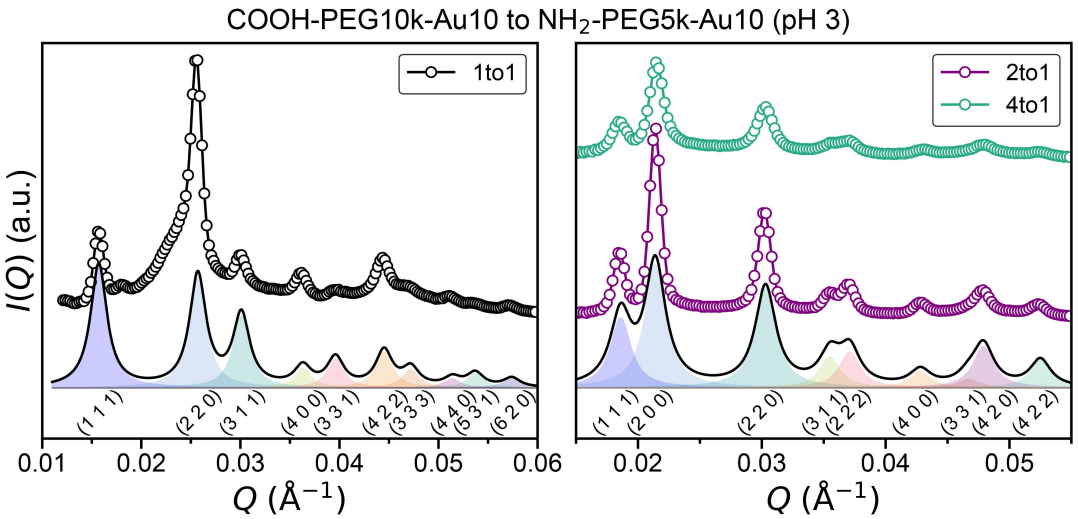

Component A	Component B	γ	θ
COOH-PEG10k-Au10	NH_2-PEG5k-Au10	0.63*	2.0
		0.97	

Mixing Ratio (A:B)	1to1	2to1	4to1
Lattice Type	Diamond	NaCl-like	NaCl-like
Lattice Constant (a_L)	~ 69 nm	~ 59 nm	~ 59 nm
A-A Nearest Neighbor (d_{NN})	~ 49 nm	~ 42 nm	~ 42 nm
A-B Nearest Neighbor (d_{NN})	~ 30 nm	~ 30 nm	~ 30 nm

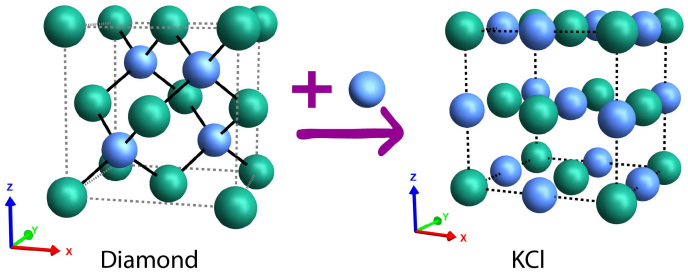

Fig. S14. SAXS diffraction patterns ($I(Q)$ vs. Q) for binary mixtures of COOH-PEG10k-Au10 and NH_2-PEG5k-Au10 at various mixing ratios, as indicated, at pH 3. (Left) The diffraction pattern for the 1:1 mixture corresponds to a diamond-like structure. The modeled intensity profile is shown below the plot, with individual peak contributions highlighted. (Right) The diffraction patterns for the 2:1 and 4:1 mixtures correspond to a NaCl-like structure. Although both mixtures contain 10 nm nanoparticles, nanoparticle fractionalization appears to create an effective size disparity, favoring the formation of a NaCl-like arrangement. The modeled intensity profiles, along with individual peak contributions, are shown below each plot. Relevant lattice parameters for each structure are summarized in the table below the plots, with schematic representations of the diamond-like and NaCl-like (rock-salt) lattices provided adjacent to the table for reference. $*$ represents the γ value estimated from the NN distance of a diamond lattice.

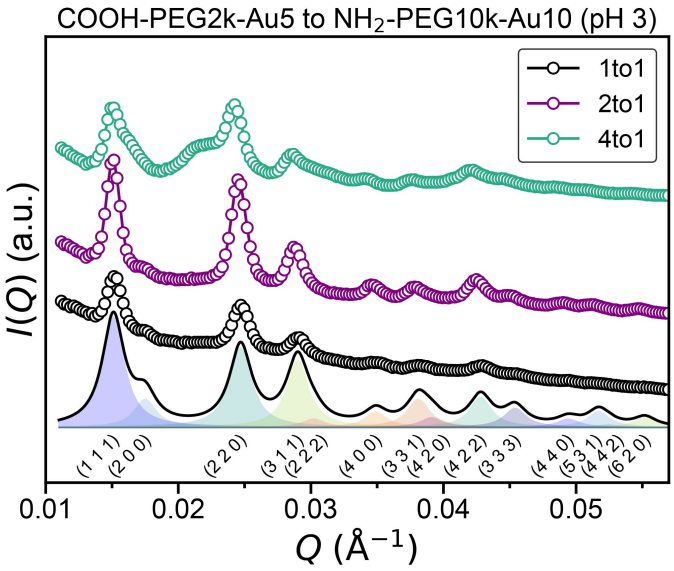

Component A	Component B	γ	θ
COOH-PEG2k-Au10	NH_2-PEG10k-Au10	0.57	0.2

Mixing Ratio (A:B)	1to1	2to1	4to1
Lattice Type	ZnS-like	ZnS-like	ZnS-like
Lattice Constant (a_L)	~ 72 nm	~ 72 nm	~ 72 nm
A-A Nearest Neighbor (d_{NN})	~ 51 nm	~ 51 nm	~ 51 nm
A-B Nearest Neighbor (d_{NN})	~ 31 nm	~ 31 nm	~ 31 nm

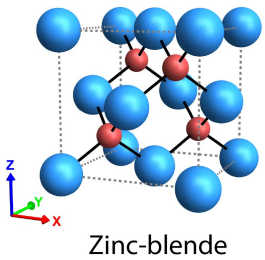

Fig. S15. SAXS diffraction patterns ($I(Q)$ vs. Q) for binary mixtures of COOH-PEG2k-Au5 and NH_2-PEG10k-Au10 at various mixing ratios, as indicated, at pH 3. The modeled intensity profiles corresponding to a zinc-blende lattice are shown as solid black lines, with individual peak contributions shaded below. The diffraction patterns for all three mixing ratios closely match the calculated diffraction pattern for a zinc-blende lattice. The green curve exhibits a subtle hump on the (220) reflection, indicative of lattice defects rather than a separate phase, since no additional discrete peaks (which would signal an impurity) are present. Relevant lattice parameters for each structure are summarized in the table adjacent to the plot, with a schematic representation of the zinc-blende lattice provided below the table for reference.

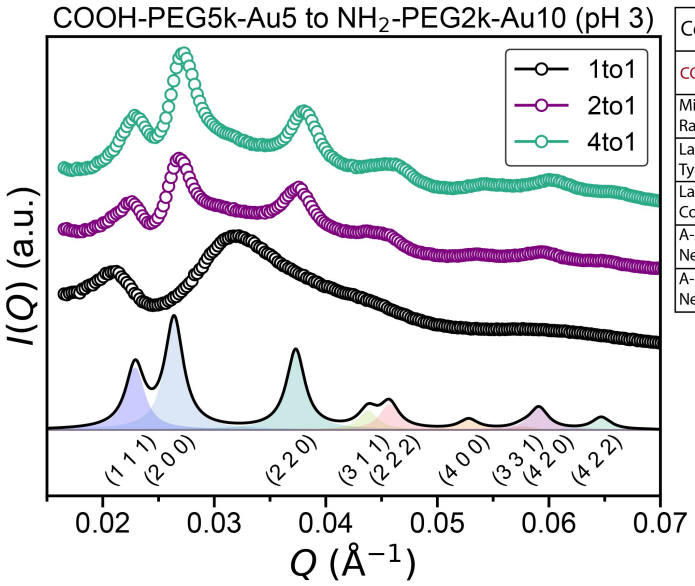

Component A	Component B	γ	θ
COOH-PEG5k-Au5	NH_2-PEG2k-Au10	0.98	2.5

Mixing Ratio (A:B)	1to1	2to1	4to1
Lattice Type	SRO	NaCl-like	NaCl-like
Lattice Constant (a_L)	---	~ 48 nm	~ 48 nm
A-A Nearest Neighbor (d_{NN})	---	~ 34 nm	~ 34 nm
A-B Nearest Neighbor (d_{NN})	~ 30 nm	~ 24 nm	~ 24 nm

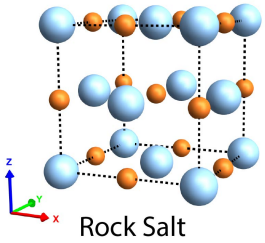

Fig. S16. SAXS diffraction patterns ($I(Q)$ vs. Q) for binary mixtures of COOH-PEG5k-Au5 and NH_2-PEG10k-Au10 at various mixing ratios, as indicated, at pH 3. The modeled intensity profiles for the 2:1 and 4:1 mixtures correspond to a rock-salt lattice, shown as solid black lines, with individual peak contributions shaded below. The diffraction pattern for the 1:1 mixture indicates a short-range ordered structure, deviating from the long-range periodicity observed in the rock-salt lattice. Relevant lattice parameters for each structure are summarized in the table adjacent to the plot, with a schematic representation of the rock-salt lattice provided below the table for reference.

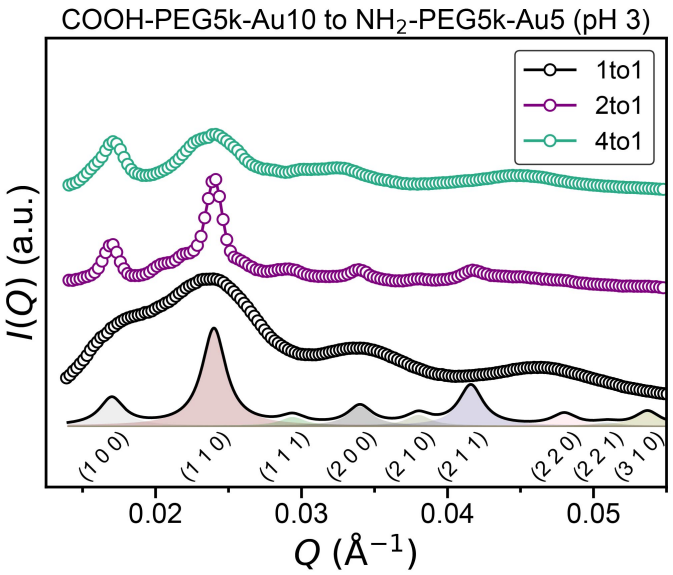

Component A	Component B	γ	θ
COOH-PEG5k-Au5	NH_2-PEG5k-Au10	0.90[#]	1.0

Mixing Ratio (A:B)	1to1	2to1	4to1
Lattice Type	CsCl-motifs	CsCl	CsCl (Distorted)
Lattice Constant (a_L)	---	~ 37 nm	~ 37 nm
A-A Nearest Neighbor (d_{NN})	---	~ 37 nm	~ 37 nm
A-B Nearest Neighbor (d_{NN})	~ 38 nm	~ 26 nm	~ 26 nm

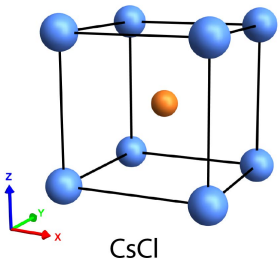

Fig. S17. SAXS diffraction patterns ($I(Q)$ vs. Q) for binary mixtures of COOH-PEG5k-Au5 and NH_2-PEG5k-Au10 at various mixing ratios, as indicated, at pH 3. The modeled intensity profile for the 2:1 mixture corresponds to a CsCl lattice, shown as solid black lines, with individual peak contributions shaded below. For the 1:1 mixture, the diffraction pattern suggests a short-range ordered structure with CsCl-like motifs, as discussed in detail in the SI. The 4:1 mixture shows broadened peaks, primarily due to lattice defects in the CsCl lattice, which are also described in the SI. Relevant lattice parameters for each structure are summarized in the table adjacent to the plot, with a schematic representation of the CsCl lattice provided below the table for reference.

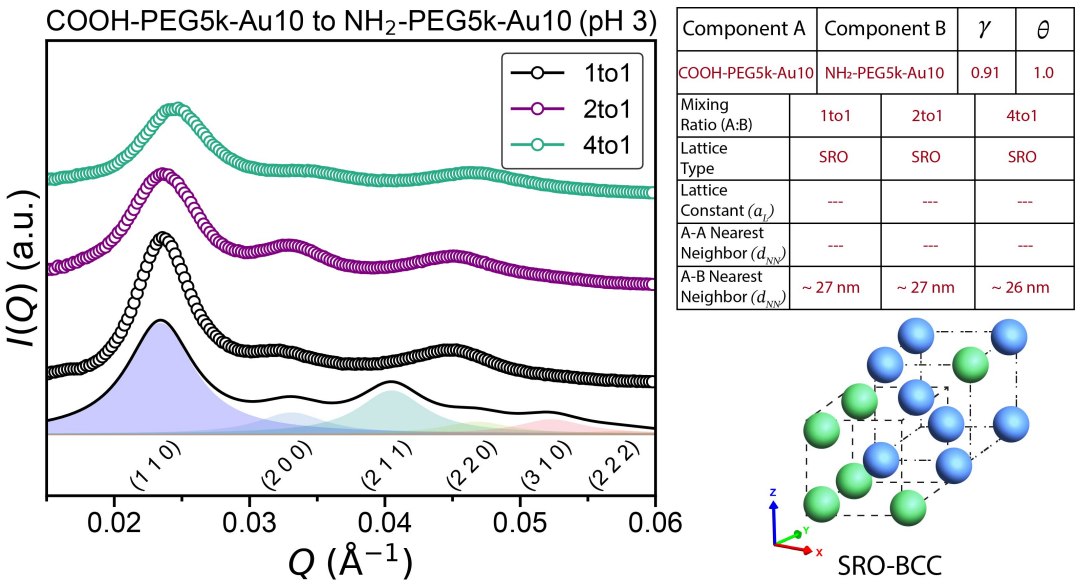

Component A	Component B	γ	θ
COOH-PEG5k-Au10	NH_2-PEG5k-Au10	0.91	1.0

Mixing Ratio (A:B)	1to1	2to1	4to1
Lattice Type	SRO	SRO	SRO
Lattice Constant (a_L)	---	---	---
A-A Nearest Neighbor (d_{NN})	---	---	---
A-B Nearest Neighbor (d_{NN})	~ 27 nm	~ 27 nm	~ 26 nm

Fig. S18. SAXS diffraction patterns ($I(Q)$ vs. Q) for binary mixtures of COOH-PEG5k-Au10 and NH_2-PEG5k-Au10 at various mixing ratios, as indicated, at pH 3. The modeled intensity profile corresponds to a BCC lattice, shown as solid black lines, with individual peak contributions shaded below. The diffraction pattern displays broadened peaks with three main maxima, but the peak positions and intensities closely match those expected for a BCC lattice. Relevant lattice parameters for each structure are summarized in the table adjacent to the plot, with a schematic representation of the BCC lattice provided below the table for reference.

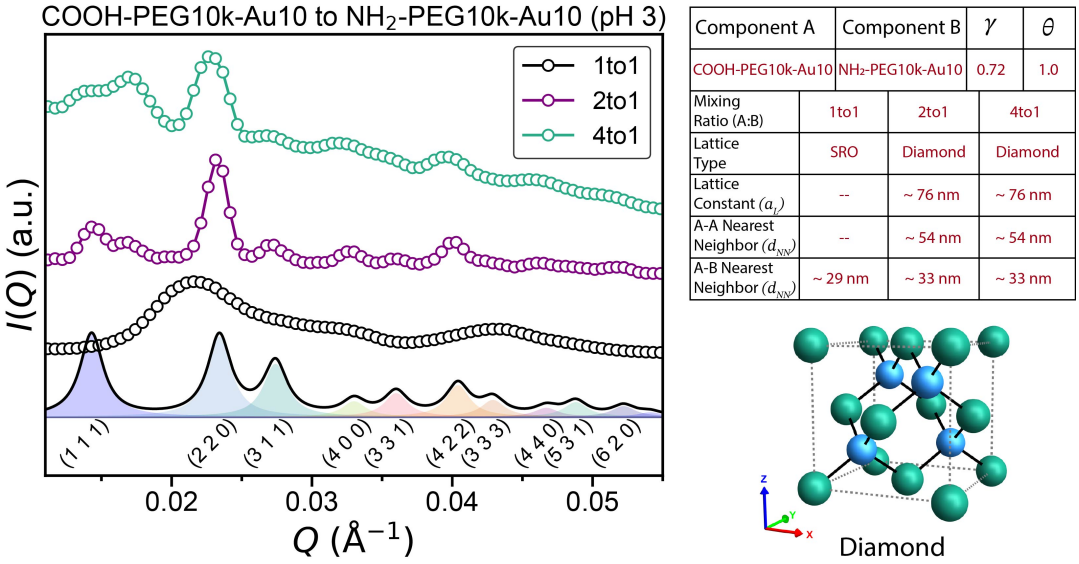

Component A	Component B	γ	θ
COOH-PEG10k-Au10	NH_2-PEG10k-Au10	0.72	1.0

Mixing Ratio (A:B)	1to1	2to1	4to1
Lattice Type	SRO	Diamond	Diamond
Lattice Constant (a_L)	--	~ 76 nm	~ 76 nm
A-A Nearest Neighbor (d_{NN})	--	~ 54 nm	~ 54 nm
A-B Nearest Neighbor (d_{NN})	~ 29 nm	~ 33 nm	~ 33 nm

Fig. S19. SAXS diffraction patterns ($I(Q)$ vs. Q) for binary mixtures of COOH-PEG10k-Au10 and NH_2-PEG10k-Au10 at various mixing ratios, as indicated, at pH 3. The modeled intensity profiles corresponding to a diamond lattice are shown as solid black lines, with individual peak contributions shaded below. The 1:1 mixture exhibits only SRO, whereas the 1:2 and 1:4 mixtures produce diffraction patterns matching a diamond lattice; notably, a peak adjacent to the diamond (111) reflection coincides with the ZnS (200) peak, indicating a fractionalization effect. Relevant lattice parameters for each structure are summarized in the table adjacent to the plot, with a schematic representation of the diamond lattice provided below the table for reference.

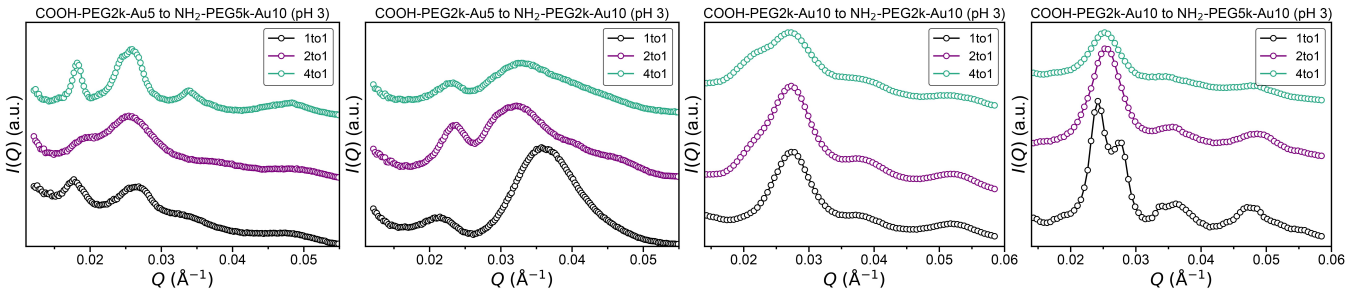

Component A	Component B	γ	θ
COOH-PEG2k-Au5	NH_2-PEG5k-Au10	0.77	0.4
Mixing Ratio (A:B)	1to1	2to1	4to1
Lattice Type	SRO	SRO	SRO
Lattice Constant (a_L)	---	---	---
A-A Nearest Neighbor (d_{NN})	---	---	---
A-B Nearest Neighbor (d_{NN})	~ 35 nm	~ 33 nm	~ 35 nm

Component A	Component B	γ	θ
COOH-PEG2k-Au5	NH_2-PEG2k-Au10	0.95	1.0
Mixing Ratio (A:B)	1to1	2to1	4to1
Lattice Type	SRO	SRO	SRO
Lattice Constant (a_L)	---	---	---
A-A Nearest Neighbor (d_{NN})	---	---	---
A-B Nearest Neighbor (d_{NN})	~ 30 nm	~ 27 nm	~ 28 nm

Component A	Component B	γ	θ
COOH-PEG2k-Au10	NH_2-PEG2k-Au10	0.94	1.0
Mixing Ratio (A:B)	1to1	2to1	4to1
Lattice Type	SRO	SRO	SRO
Lattice Constant (a_L)	---	---	---
A-A Nearest Neighbor (d_{NN})	---	---	---
A-B Nearest Neighbor (d_{NN})	~ 23 nm	~ 24 nm	~ 25 nm

Component A	Component B	γ	θ
COOH-PEG2k-Au5	NH_2-PEG5k-Au10	0.86	0.4
Mixing Ratio (A:B)	1to1	2to1	4to1
Lattice Type	SRO	SRO	SRO
Lattice Constant (a_L)	---	---	---
A-A Nearest Neighbor (d_{NN})	---	---	---
A-B Nearest Neighbor (d_{NN})	~ 30 nm	~ 27 nm	~ 28 nm

Fig. S20. SAXS diffraction patterns ($I(Q)$ vs. Q) for binary mixtures of (a) COOH-PEG2k-Au5 and NH_2-PEG5k-Au10 (b) COOH-PEG2k-Au5 and NH_2-PEG2k-Au10 (c) COOH-PEG2k-Au10 and NH_2-PEG2k-Au10 (d) COOH-PEG2k-Au5 and NH_2-PEG5k-Au10 at various mixing ratios, as indicated, at pH 3. The diffraction pattern displays broadened peaks with three main maxima that only give information about the characteristic NN distance. We note that some diffraction patterns display more than four peaks indicative of meso-range ordering, but these features alone are insufficient to unambiguously assign a specific structure. Relevant lattice parameters for each structure are summarized in the table below, along with the plots.

To further validate the robustness of our self-assembly strategy, we extended our investigation to binary mixtures with different NPs sizes. In addition to the 10 nm and 5 nm systems, we explored mixtures composed of 20 nm and 10 nm nanoparticles, both functionalized with PEG chains terminated with charged end groups. By carefully adjusting the mixing ratios to maintain similar effective size ratios (γ) and ligand molecular weight ratios (θ), we observed that the larger nanoparticles self-assemble into the same zinc-blende (ZnS-like) superlattice as their smaller counterparts. SAXS diffraction patterns in Fig. S21 confirm that the structural features of the ZnS lattice are preserved across different NP size combinations.

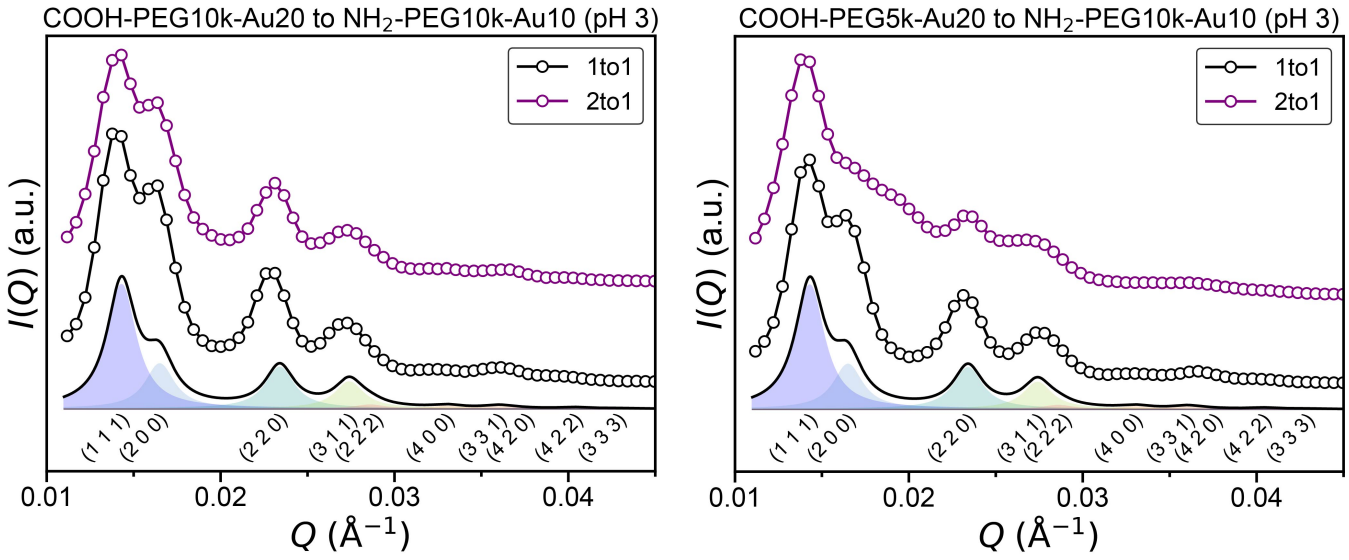

Fig. S21. SAXS diffraction patterns ($I(Q)$ vs. Q) for binary mixtures of (a) COOH-PEG10k-Au20 and NH_2-PEG10k-Au10 (b) COOH-PEG5k-Au20 and NH_2-PEG10k-Au10 at various mixing ratios, as indicated, at pH 3. The modeled intensity profiles corresponding to a zinc-blende lattice are shown as solid black lines, with individual peak contributions shaded below. The diffraction patterns for all mixing ratios closely match the calculated diffraction pattern for a zinc-blende lattice. This figure demonstrates that our strategy can be applied to nanoparticle systems of various sizes to form ionic superlattices while maintaining the key parameters γ and θ.

SAXS data analysis

The form factor amplitude for a single solid sphere of electron density ρ and diameter D is as follows:

$$f(Q) = 3\rho v \frac{\sin(QD/2) - QD/2 \times \cos(QD/2)}{(QD/2)^3} \tag{S2}$$

where v is the volume of the sphere, i.e., $\pi D^3/6$. The ratio of the form factor amplitude for particle $\mathcal{A}$ of $D = 95$ Å and $\mathcal{B}$ of $D = 65$ Å, $f_\mathcal{A}$ and $f_\mathcal{B}$ at $Q = 0$ is,

$$\frac{f_\mathcal{B}}{f_\mathcal{A}} = 65^3/95^3 \approx 0.32 \tag{S3}$$

Each lattice point is associated with a basis of formula $\mathcal{A}_m\mathcal{B}_n$. Their fractional coordinates in the unit cell are denoted as $(u_{A,i}, v_{A,i}, w_{A,i})$ and $(u_{B,i}, v_{B,i}, w_{B,i})$, where the subscript i runs up to m and n for A and B, respectively. The unit cell structure factor F_{hkl} is expressed as follows:

$$F_{hkl} = \{f_\mathcal{A} \sum_{i=1}^{m} \exp\left[-j2\pi(hu_{\mathcal{A},i} + kv_{\mathcal{A},i} + lw_{\mathcal{A},i})\right] + f_\mathcal{B} \sum_{i=1}^{n} \exp\left[-j2\pi(hu_{\mathcal{B},i} + kv_{\mathcal{B},i} + lw_{\mathcal{B},i})\right]\} \tag{S4}$$

For SAXS where the scattering angles are small, The observed Bragg reflection intensity for Miller indices (h, k, l), denoted as I_{hkl}, is proportional to $|F_{hkl}|^2$

$$I_{hkl} \propto |F_{hkl}|^2 \times m_{hkl}/Q_{hkl}^2, \tag{S5}$$

where m_{hkl} represents the multiplicity at each peak position Q_{hkl}, and Q_{hkl}^{-2} is proportional to Lorentz factor for powder diffraction with Debye-Scherrer geometry at low scattering angle limit.

For a cubic system, the peak position Q_{hkl} depends on the unit cell length, a, as below,

$$Q_{hkl} = 2\pi\sqrt{h^2 + k^2 + l^2}/a. \tag{S6}$$

In certain cases, even though we use two different nanoparticles with opposite charges, their cores remain identical. As a result, Eq. S4 simplifies further, since $f_\mathcal{A} = f_\mathcal{B} = f$, reducing Eq. S5 to:

$$I_{hkl} \propto f^2 \times \frac{m_{hkl}}{Q_{hkl}^2}, \tag{S7}$$

ZnS Structure

For a ZnS (Zinc Blende) structure, the atoms $\mathcal{A}$ (Zn) and $\mathcal{B}$ (S) per unit cell are located at:

$$\mathcal{A} \text{ (Zn) at } \left\{(0,0,0), \left(\frac{1}{2},\frac{1}{2},0\right), \left(\frac{1}{2},0,\frac{1}{2}\right), \left(0,\frac{1}{2},\frac{1}{2}\right)\right\}$$

$$\mathcal{B} \text{ (S) at } \left\{\left(\frac{1}{4},\frac{1}{4},\frac{1}{4}\right), \left(\frac{3}{4},\frac{3}{4},\frac{1}{4}\right), \left(\frac{3}{4},\frac{1}{4},\frac{3}{4}\right), \left(\frac{1}{4},\frac{3}{4},\frac{3}{4}\right)\right\}$$

The Eq.S4 for the ZnS (Zinc Blende) structure is given by:

$$|F_{hkl}|^2 = \begin{cases} 16(f_\mathcal{A} + f_\mathcal{B})^2, & \text{if } (h+k+l) \text{ is an even multiple of 2} \\ 16(f_\mathcal{A} - f_\mathcal{B})^2, & \text{if } (h+k+l) \text{ is an odd multiple of 2} \\ 16(f_\mathcal{A}^2 + f_\mathcal{B}^2) & \text{for all odd } h,k,l \\ 0, & \text{for mixed } h,k,l \end{cases} \tag{S8}$$

Table S2: Calculated (h,k,l) peak intensity I_{hkl} for a ZnS structure with unit cell edge length $a = 76$ nm. Q_0 represents the peak 100 position for a cubic lattice.

hkl	Q_{hkl}/Q_0	m_{hkl}	$m_{hkl}/(Q_{hkl}/Q_0)^2$	I_{hkl}
111	$\sqrt{3}$	8	2.7	100.0
200	2	6	1.5	22.0
220	$\sqrt{8}$	12	1.5	78.1
311	$\sqrt{11}$	24	2.2	64.3
222	$\sqrt{12}$	8	0.7	7.1
400	4	6	0.4	15.6
331	$\sqrt{19}$	24	1.3	29.1
420	$\sqrt{20}$	24	1.2	8.9

Diamond Structure

The Diamond cubic structure is essentially an FCC lattice with a two-atom basis, similar to ZnS, but where both atoms are the same type (C, Si, or Ge, etc.) instead of Zn and S.

For a Diamond structure, the atomic positions per unit cell are:

$$\mathcal{A} \text{ at } \left\{(0,0,0), \left(\frac{1}{2},\frac{1}{2},0\right), \left(\frac{1}{2},0,\frac{1}{2}\right), \left(0,\frac{1}{2},\frac{1}{2}\right)\right\}$$

$$\mathcal{B} \text{ at } \left\{\left(\frac{1}{4},\frac{1}{4},\frac{1}{4}\right), \left(\frac{3}{4},\frac{3}{4},\frac{1}{4}\right), \left(\frac{3}{4},\frac{1}{4},\frac{3}{4}\right), \left(\frac{1}{4},\frac{3}{4},\frac{3}{4}\right)\right\}$$

The Eq.S4 for the Diamond structure is given by:

$$|F_{hkl}|^2 = \begin{cases} 64f^2, & \text{if } h,k,l \text{ are all even and } h+k+l \equiv 0 \pmod 4 \\ 0, & \text{if } h,k,l \text{ are all even and } h+k+l \equiv 2 \pmod 4 \\ 32f^2, & \text{if } h,k,l \text{ are all odd} \\ 0, & \text{if } h,k,l \text{ are mixed} \end{cases} \tag{S9}$$

Table S3: Calculated (h,k,l) peak intensity I_{hkl} for a diamond structure with unit cell edge length $a = 79$ nm, and constituent particle size $D = 95$ nm. Q_0 represents the peak 100 position for a cubic lattice.

hkl	Q_{hkl}/Q_0	m_{hkl}	$m_{hkl}/(Q_{hkl}/Q_0)^2$	I_{hkl}
111	$\sqrt{3}$	8	2.7	100.0
220	$\sqrt{8}$	12	1.5	97.2
311	$\sqrt{11}$	24	2.2	64.7
400	$\sqrt{16}$	6	0.4	19.1
331	$\sqrt{19}$	24	1.3	29.3
422	$\sqrt{24}$	24	1.0	39.6

NaCl Structure

For a NaCl (rock salt) structure, the atoms $\mathcal{A}$ (Na) and $\mathcal{B}$ (Cl) per unit cell are located at:

$$\mathcal{A} \text{ (Na) at } \left\{(0,0,0), \left(\frac{1}{2},\frac{1}{2},0\right), \left(\frac{1}{2},0,\frac{1}{2}\right), \left(0,\frac{1}{2},\frac{1}{2}\right)\right\}$$

$$\mathcal{B}\ (\text{Cl})\ \text{at}\ \left\{\left(\frac{1}{2},\frac{1}{2},\frac{1}{2}\right),\left(0,\frac{1}{2},0\right),\left(0,0,\frac{1}{2}\right),\left(\frac{1}{2},0,0\right)\right\}$$

The Eq.S4 for the NaCl (rock salt) structure is given by:

$$F_{hkl}=\begin{cases}4(f_{\mathcal{A}}+f_{\mathcal{B}}), & \text{for all even } h,k,l\\ 4(f_{\mathcal{A}}-f_{\mathcal{B}}), & \text{for all odd } h,k,l\\ 0, & \text{for mixed } h,k,l\end{cases} \tag{S10}$$

Table S4: Calculated (h,k,l) peak intensity I_{hkl} for a NaCl structure with unit cell edge length $a = 65$ nm. Q_0 represents the peak 100 position for a cubic lattice.

hkl	Q_{hkl}/Q_0	m_{hkl}	$m_{hkl}/(Q_{hkl}/Q_0)^2$	I_{hkl}
111	$\sqrt{3}$	8	2.7	46.5
200	2	6	1.5	100.0
220	$\sqrt{8}$	12	1.5	86.0
311	$\sqrt{11}$	24	2.2	24.1
222	$\sqrt{12}$	8	0.7	32.7
400	4	6	0.4	15.7
331	$\sqrt{19}$	24	1.3	8.5
420	$\sqrt{20}$	24	1.2	43.0

Simple Cubic Structure

For a Simple Cubic (SC) structure, the atoms per unit cell are located at:

$$\mathcal{A}\ \text{at}\ (0,0,0)$$

The Eq.S4 for the Simple Cubic structure is given by:

$$F_{hkl}=f,\quad \text{for all } h,k,l \tag{S11}$$

Table S5: Calculated (h,k,l) peak intensity I_{hkl} for a simple cubic structure with unit cell edge length $a = 33$ nm and constituent particle size $D = 95$ nm. Q_0 represents the peak 100 position for a cubic lattice.

hkl	Q_{hkl}/Q_0	m_{hkl}	$m_{hkl}/(Q_{hkl}/Q_0)^2$	I_{hkl}
100	$\sqrt{1}$	6	6.0	100.0
110	$\sqrt{2}$	12	6.0	84.4
111	$\sqrt{3}$	8	2.7	31.5
200	$\sqrt{4}$	6	1.5	14.8
210	$\sqrt{5}$	24	4.8	39.4
211	$\sqrt{6}$	24	4.0	27.2

CsCl structure

For a CsCl structure, the atoms $\mathcal{A}$ (Cs) and $\mathcal{B}$ (Cl) per unit cell are located at:

$$\mathcal{A}\ (\text{Cs})\ \text{is located at}\ (0,0,0)$$

$$\mathcal{B}\ (\mathrm{Cl})\ \text{is located at}\ \left(\frac{1}{2},\frac{1}{2},\frac{1}{2}\right)$$

The Eq.S4 is reduced to

$$F_{hkl} = \begin{cases} f_{\mathcal{A}} - f_{\mathcal{B}}, & \text{if } h+k+l = \text{odd} \\ f_{\mathcal{A}} + f_{\mathcal{B}}, & \text{if } h+k+l = \text{even} \end{cases} \tag{S12}$$

The calculated intensities for each hkl peak is listed in Table S6.

Table S6: Calculated (h,k,l) peak intensity I_{hkl} for the CsCl structure.

hkl	Q_{hkl}/Q_0	m_{hkl}	$m_{hkl}/(Q_{hkl}/Q_0)^2$	I_{hkl}
100	1	6	6	29.2
110	$\sqrt{2}$	12	6	100.0
111	$\sqrt{3}$	8	2.7	7.6
200	2	6	1.5	17.4
210	$\sqrt{5}$	24	4.8	7.4
211	$\sqrt{6}$	24	4	31.6
220	$\sqrt{8}$	12	1.5	8.0

It is worth noting that there are two satellite peaks symmetrically located around peak $(1,1,0)$ at $Q_{110} \pm q$, where $q \approx 0.0025$ Å^{-1}, as indicated by two vertical dashed lines in Fig.S23 (a). There are two interpretations as briefly and heuristically discussed below.

Finite crystal size

If the super-lattice is confined within the length of L in a particular direction, the Bragg reflection peak along this direction shall be shaped approximately as a squared *sinc* function, namely,

$$\frac{\sin[(Q-Q_{hkl})L/2]^2}{[(Q-Q_{hkl})L/2]^2} \tag{S13}$$

which yields fringes symmetrically around central main Bragg reflection at Q_{hkl}. The two maximum located at $Q_{hkl} \pm q$ where $q = 2\pi/L$. Therefore, it is estimated that superlattice is confined within $L \approx 250$ nm along [110] direction, which is the shortest dimension of the crystal. This also suggests that orderly stacking of $\{1,1,0\}$ planes in $\langle 110 \rangle$ direction are confined in $L/d_{110} = Q_{hkl}/q \approx 11$ layers.

Modulated crystal

If the superlattice inter-plance distances, i.e., d_{hkl}, is modulated with a wavelength λ_m, e.g., $\cos(2\pi d_{hkl} n)$ where n is the n-th plane in the stack, there will emerge satellite peaks at $Q_{hkl} \pm q$ where $q = 2\pi/\lambda_m$. Again, here $\lambda_m \approx 250$ nm, across approximately 11 unit cells.

The position vector of n-th unit cell can be expressed as

$$\vec{r_n} = n_1\vec{a} + n_2\vec{b} + n_3\vec{c}. \tag{S14}$$

where $\vec{a}$, $\vec{b}$ and $\vec{c}$ are basis vectors. n_1, n_2, n_3 are integers.

Now introduce a modulated, small displacement perturbation of magnitude u, much less than the unit cell length, along unit direction vector $\vec{m}$, i.e.,

$$\vec{r} = \vec{r}_n + u\vec{m}\cos(2\pi\vec{r}_n \cdot \vec{m}/\lambda_m) \tag{S15}$$

The phase factor $e^{i\vec{Q}\cdot\vec{r}}$ can be factored into:

$$\exp\left[i\vec{Q}\cdot\vec{r}\right] \approx \exp\left[i\vec{Q}\cdot\vec{r}_n\right] + \frac{iu\vec{Q}\cdot\vec{m}}{2}\left\{\exp\left[i(\vec{Q}-\vec{q})\cdot\vec{r}_n\right] + \exp\left[i(\vec{Q}+\vec{q})\cdot\vec{r}_n\right]\right\} \tag{S16}$$

where $\vec{q} = 2\pi\vec{m}/\lambda_m$.

Integrating the phase factors over the entire lattice, i.e., $\sum_{n_1,n_2,n_3}\exp\left[i\vec{Q}\cdot\vec{r}\right]$, yeilds Bragg reflection peaks at $\vec{Q}_{hkl}$, and $\vec{Q}_{hkl} \pm \vec{q}$.

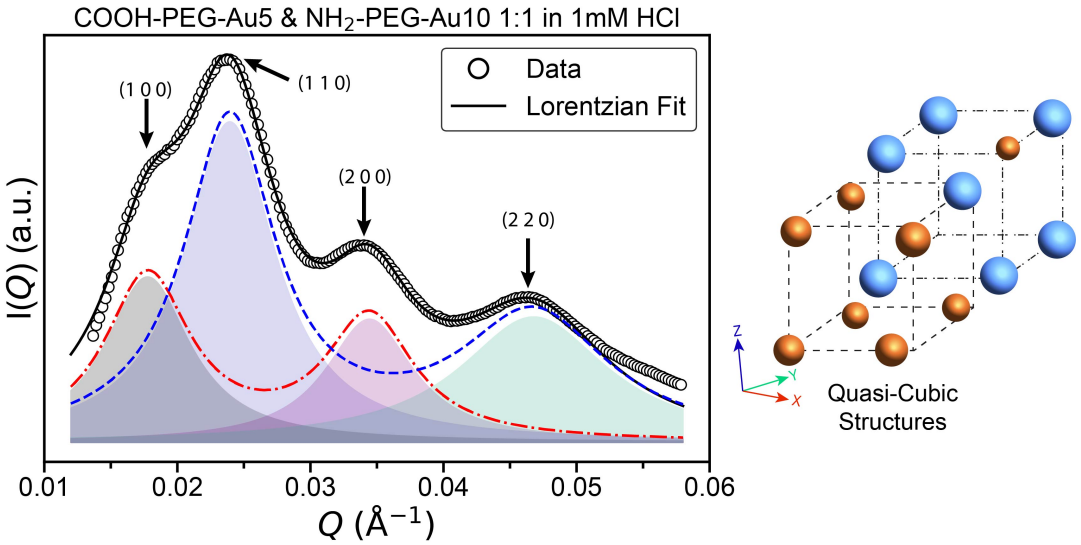

Fig. S22. SAXS diffraction data for 1:1 mixture of NH_2-PEG-AuNP10 and COOH-PEG-AuNP5 at room temperature. The black solid line represents a Lorentzian fit for the overall scattering profile. The red dashed line corresponds to the Lorentzian fit for the 100 1-D structure, while the blue dash-dot line represents the fit for the 110 1-D structure. The peak ratio for the first two peaks is $\sqrt{2}$, indicating geometric scaling equivalent to a cubic lattice; the third peak is exactly double that of the first, and the fourth peak is twice the second, consistent with the ordered structural repetition in the scattering pattern for 1D-like structures. A schematic illustration of a Quasi-cubic structure is provided next to the plot.

Lattice distortion

The lattice can be distorted slightly so that the lattice parameter $(a, b, c, \alpha, \beta, \gamma)$ deviates from $a = b = c$ and $\alpha = \beta = \gamma = 90°$ that is for cubic symmetry. This distortion lead to Bragg reflection split. The simplest case is the cubic distorted to tetragonal lattice, i.e., $a = b \neq c$. In this case, the peak 110 in the cubic system will split into two peaks with intensity ratio $2:1$ as planes (101) and (011) are equivalent, and (110) is nonequivalent.

For tetragonal system, assume the lattice parameter is $a = a^*$ and $c = c^*$,

$$Q_{101}^2/4\pi^2 = \left(\frac{1}{a^{*2}} + \frac{1}{c^{*2}}\right) \tag{S17}$$

$$Q_{110}^2/4\pi^2 = \frac{2}{a^{*2}} \tag{S18}$$

Let $\bar{Q} = (Q_{110} + Q_{101})/2$, $q = (Q_{110} - Q_{101})/2$, where $\bar{Q} \gg q$, we have

$$a^* \approx \sqrt{2}\frac{2\pi}{\bar{Q}}(1 - q/\bar{Q}) \tag{S19}$$

$$c^* \approx \sqrt{2}\frac{2\pi}{\bar{Q}}(1 + 3q/\bar{Q}) \tag{S20}$$

Substitute $\bar{Q}$ with 0.0294Å^{-1} and q with 0.0025Å^{-1}, we have $a^* \approx 27$ nm, and $c^* \approx 38$ nm.

Indeed, if part of all cubic lattices transit to tetragonal, all main Bragg reflection peaks shown in Fig.S23 (a) will be clustered with satellite peaks. For instance, the (100), (200), (220) and (211) will split into a doublet, with a relative intensity ratio 2:1, and (210) into a triplet. However, they are too weak compared to the original peak to be visible.

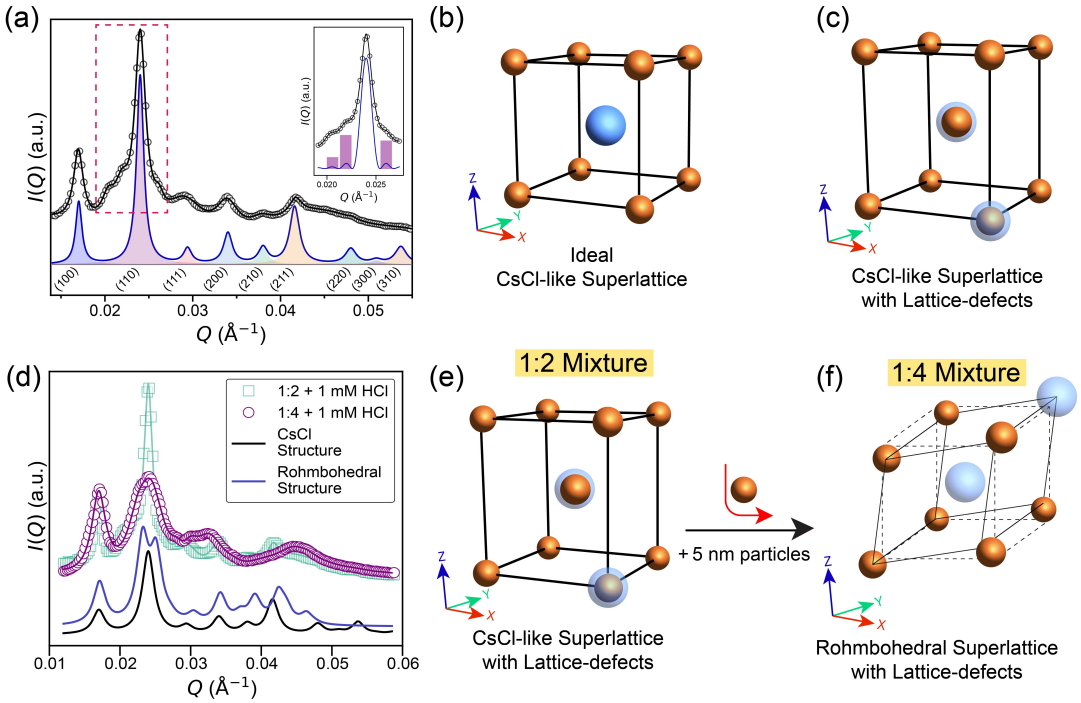

Fig. S23. (a) SAXS intensity profiles $I(Q)$ as a function of the scattering vector Q for a 1:2 mixture of NH_2-PEG5k-Au10 and COOH-PEG5k-Au5 at pH 3. Two satellite peaks near the (110) peak (highlighted in the red box) emerge due to lattice elongation or substitution, as illustrated schematically in (b) and (c). The inset shows a calculated intensity profile for a modulated CsCl-like superlattice with secondary tetragonal distortion, as discussed in detail in the Supporting Information (SI). (d) Comparison of diffraction patterns: The CsCl-like pattern for the 1:2 molar ratio mixture (□, reproduced from Fig. S17) is overlaid with the pattern for the 1:4 molar ratio mixture (◯) at pH 3 (1 mM HCl). The diffraction pattern for the 1:4 mixture is interpreted as a distorted rhombohedral-like structure, resulting from site-mixing within the original CsCl-like motif. This interpretation is supported by the broadening of the primary (111) peak and the increased intensity of weak satellite peaks observed in the 1:2 mixture. We present two calculated structure factors to validate this structural interpretation: one for the ideal CsCl-like structure (black solid line) and another for an ideal rhombohedral structure (blue solid line). Both calculations use a lattice parameter of $a = 37$ nm, with the rhombohedral structure having an angle $\alpha = 85°$. (e) and (f) Schematic illustrations of the structural transition from the CsCl-like superstructure to the distorted rhombohedral-like structure, driven by site-mixing.

Table S7: Lattice Parameters and Nearest Neighbor Distances

Lattice Type	Space Group	q_0 $(h\,k\,l)$	A-A Nearest Neighbor	A-B Nearest Neighbor	A-A NN Distance	A-B NN Distance
ZnS	216	(1 1 1)	(1/2, 1/2, 0)	(1/4, 1/4, 1/4)	$a_L/\sqrt{2}$	$\sqrt{3}a_L/4$
Diamond	227	(1 1 1)	(1/2, 1/2, 0)	(1/4, 1/4, 1/4)	$a_L/\sqrt{2}$	$\sqrt{3}a_L/4$
NaCl	225	(1 1 1)	(1/2, 1/2, 0)	(1/2, 0, 0)	$a_L/\sqrt{2}$	$a_L/2$
Simple Cubic	225	(1 0 0)	(1/2, 1/2, 0)	(1/2, 0, 0)	$\sqrt{2}a_L$	a_L
CsCl	221	(1 0 0)	(1, 0, 0)	(1/2, 1/2, 1/2)	a_L	$\sqrt{3}a_L/2$

* a_L is lattice constant of a lattice

Derived Simple Cubic Structure

In the simple cubic structure reported here, the arrangement is derived from a NaCl-type lattice. In our system, both the positive and negative sites are occupied by 10 nm core AuNPs rather than by particles of different sizes (e.g., 5 ,nm and 10 nm as in conventional NaCl). Although these oppositely charged AuNPs follow the same principles that lead to a rock-salt structure, X-ray scattering cannot differentiate between the identical 10 nm cores or the PEG grafted to them. As a result, the diffraction pattern exhibits a simple cubic symmetry. Specifically, the weak (111) reflection characteristic of NaCl is canceled out, and the effective unit cell is reduced to half the size of a typical NaCl unit cell (see Fig. S12).

In several samples assembled under conditions expected to yield simple cubic (SC) lattices, we consistently observe the emergence of a weak but reproducible superlattice reflection at positions consistent with the (111) peak, a feature forbidden in ideal SC symmetry but allowed in NaCl- or KCl-type structures. This indicates that the self-assembled lattice adopts a binary character, despite being derived from a nominally monodisperse population of nanoparticles. We interpret this as evidence of emergent particle fractionalization, in which small but intrinsic variations in nanoparticle core size, grafting density, or surface charge result in effective symmetry breaking during assembly. The system spontaneously selects and partitions particles into two distinguishable subpopulations (A and B), which occupy the alternating sites of a rock-salt–like lattice. Notably, this behavior is not a synthesis artifact, nor is it indicative of lattice polymorphism or structural disorder: the Bragg reflections are sharp, well-defined, and consistent with a single-phase lattice. Rather, this sorting behavior appears to be an inherent feature of the assembly process itself, reflecting the system's sensitivity to subtle physico-chemical variations and the interplay between entropic and electrostatic forces. Such emergent substructure from a chemically uniform population has few analogs in nanoparticle crystallization and points to an intriguing route toward engineered binary lattices without explicitly mixing different particle types.

Lorentzian-shaped Peak Fitting

A Lorentzian-shaped peak function (Eq. S21) is used to fit the SAXS data presented in Figs 2 and 3. The peak center value obtained from the fitted function is subsequently used to determine the lattice constants, which are reported in the corresponding figures in the SI.

$$I(q) = I_0 \times \frac{2}{\pi\ w_q} \times \left(1 + 4 \times \left(\frac{q - q_c}{w_q}\right)^2\right)^{-1}, \tag{S21}$$

where I_0 is the maximum amplitude of the peak, w_q is the FWHM, q_c is the peak center position, and q is the variable q range.

pH-dependant Assembled Structure

Fig. S24 presents the SAXS diffraction patterns for binary mixtures of COOH-PEG5k-Au5 and NH_2-PEG5k-Au10 at various mixing ratios (1:1, 2:1, and 4:1) and pH values (4, 3, and 2). It is evident that LRO assemblies predominantly form at pH 3, whereas liquid-like SRO is observed at pH 2. At pH 4, SRO with cubic-like motifs emerges.

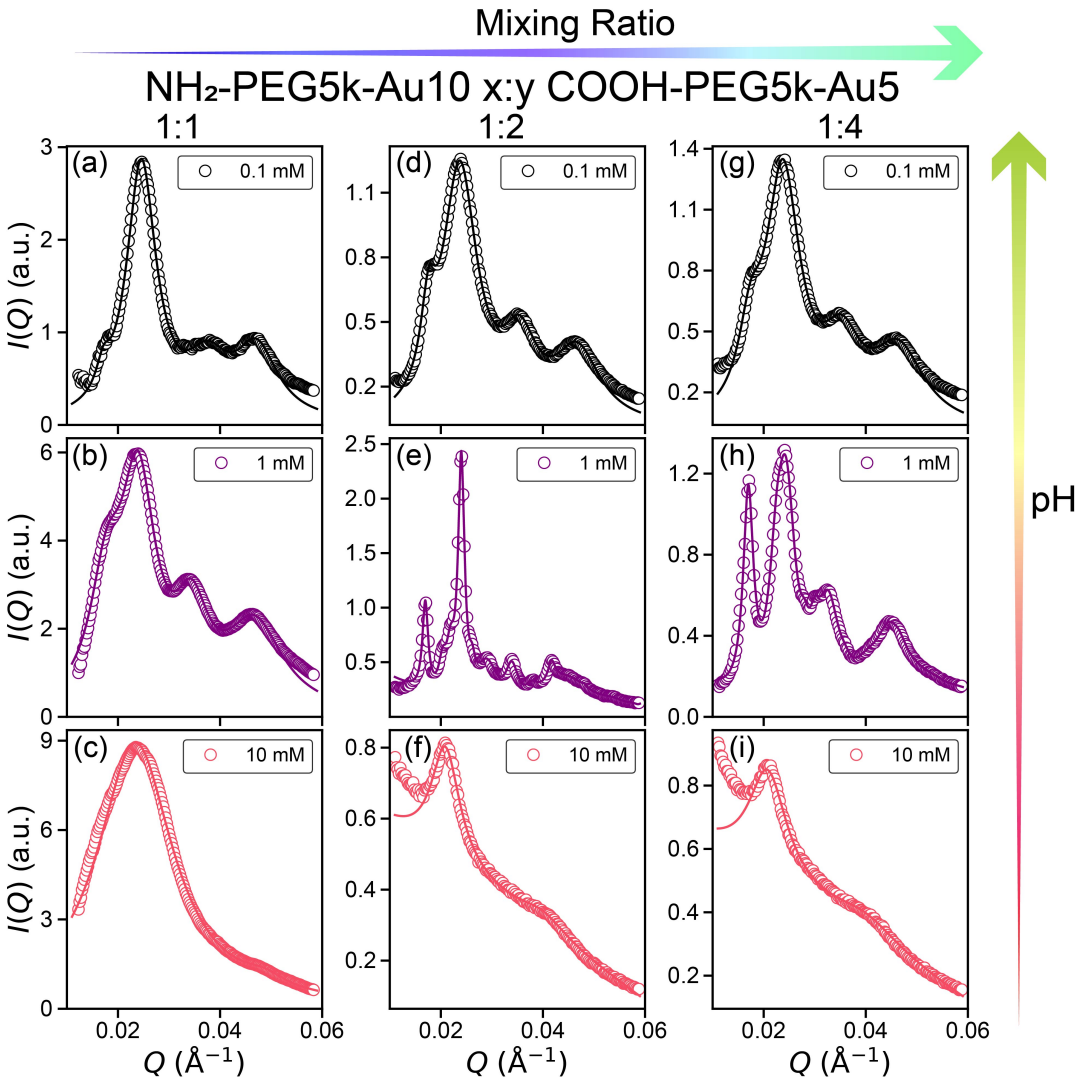

Fig. S24. SAXS intensity profiles, $I(Q)$, as a function of the scattering vector Q for binary mixtures of NH_2-PEG5k-Au10 and COOH-PEG5k-Au5 at different stoichiometric ratios and various pH values, as indicated. At pH 4, the assembly exhibits predominantly SRO, with only characteristic peaks indicative of a pre-phase. In contrast, polycrystalline LRO diffraction patterns emerge at pH 3, while at pH two the structure resembles a liquid state.

Properties of PEG

Notations and Parameter values

Table S8: Notation used in this study.

quantity	definition	notation
number of chains	chains per nanoparticle	$\mathcal{N}_p$
moles	number of moles	n
polymerization degree	number of monomers	N
density	mass/volume	ρ
specific volume	volume/mass	$\mathbb{v}$
molar volume	volume/moles	υ
number density	moles/volume	n
volume fraction	volume/volume	ϕ
molecular weight	mass/mole	M
grafting density	number of molecules/Area	σ

Following our previous studies,[31] the value of the different parameters are as given in Table S9.

Table S9: Parameters used

Definition	notation	value
PEO monomer length	l_P	3.64 (Å)
PEO Kuhn length	b	7.24 (Å)
PEO diameter factor	ν	0.584
PEO Molecular Weight	$\mathrm{M_{PEO}}$	44.052 (g·mol^{-1})
Water molecular volume	υ	29.91 (Å^3)
Nanoparticle radius	R	25.0, 45.36 (Å)
gold molecular weight	$\mathrm{M_{Au}}$	196.97 (g·mol^{-1})

The nanoparticle radius is obtained from the X-ray analysis. These parameters imply

$$\begin{aligned} \upsilon_P &= b^3\nu^2 = 129.43 \text{ Å}^3 && \text{(S22)} \\ \rho_{\mathrm{PEO}} &= 10^4 \frac{M_{\mathrm{PEO}}}{6.0221\upsilon_p}\frac{b}{l_P} = 1124 \text{ kg}\cdot\text{m}^{-3} && \text{(S23)} \\ A_c &= b^2\nu^2 = 17.88 \text{ Å}^2 && \text{(S24)} \\ N_r &= \frac{M_p}{M_{\mathrm{PEO}}} && \text{(S25)} \\ N &= 0.503 N_r \ . && \text{(S26)} \end{aligned}$$

and also $\rho_{\mathrm{Au}} = 19300$ kg·m^{-3}. Here N is the number of Kuhn segments and N_r the number of actual segments. For PEG5k, PEG2k, $M_p = 5\cdot 10^3, 2\cdot 10^3$ and hence

$$\begin{aligned} N^{\mathrm{PEG5k}} &= 57.1 \quad , \quad N_r^{\mathrm{PEG5k}} = 113.5 \\ N^{\mathrm{PEG2k}} &= 22.8 \quad , \quad N_r^{\mathrm{PEG2k}} = 45.4 \end{aligned} \qquad \text{(S27)}$$

The grafting density and number of chains per nanoparticle is

$$\begin{aligned}
\sigma^{\mathrm{PEG2k}}(D=5) &= 0.0167\frac{\mathrm{chains}}{\mathring{\mathrm{A}}^2} = 1.67\frac{\mathrm{chains}}{\mathrm{nm}^2} \rightarrow \mathcal{N}_p = 131 \\
\sigma^{\mathrm{PEG5k}}(D=5) &= 0.0279\frac{\mathrm{chains}}{\mathring{\mathrm{A}}^2} = 2.79\frac{\mathrm{chains}}{\mathrm{nm}^2} \rightarrow \mathcal{N}_p = 220 \\
\sigma^{\mathrm{PEG2k}}(D=10) &= 0.0284\frac{\mathrm{chains}}{\mathring{\mathrm{A}}^2} = 2.84\frac{\mathrm{chains}}{\mathrm{nm}^2} \rightarrow \mathcal{N}_p = 734 \\
\sigma^{\mathrm{PEG5k}}(D=10) &= 0.0183\frac{\mathrm{chains}}{\mathring{\mathrm{A}}^2} = 1.83\frac{\mathrm{chains}}{\mathrm{nm}^2} \rightarrow \mathcal{N}_p = 473
\end{aligned} \tag{S28}$$

these values are consistent with previous estimates.

Stability and Packing Fraction in CsCl, NaCl and ZnS

As a first approximation, we model the NPS as large (A) and small (B) hard spheres of diameters D_A, D_B, with the charge located at its centers.

Electrostatic Free Energy

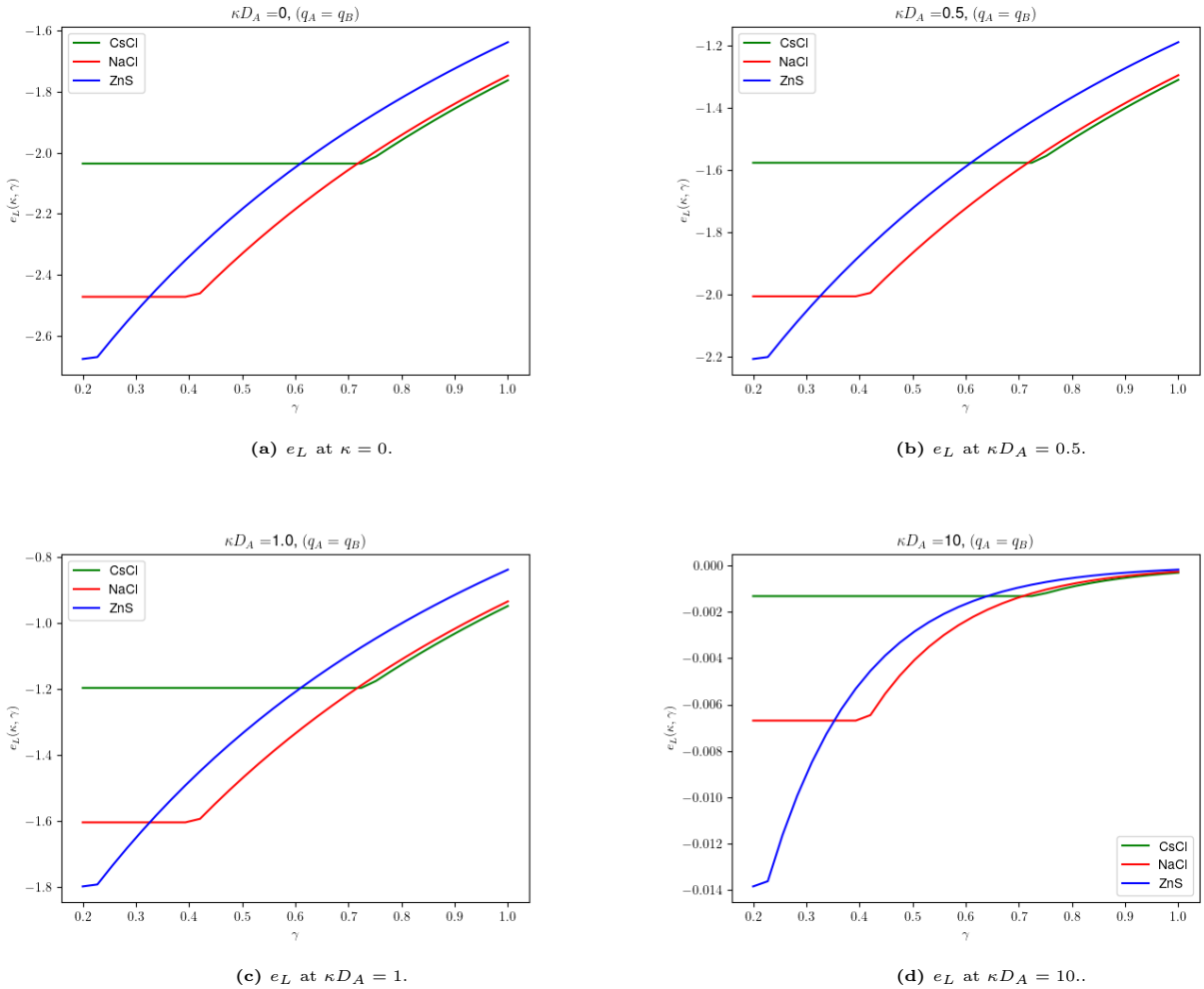

(a) e_L at $\kappa = 0$.

(b) e_L at $\kappa D_A = 0.5$.

(c) e_L at $\kappa D_A = 1$.

(d) e_L at $\kappa D_A = 10.$.

Fig. S25. e_L defined in Eq. S33 for different superlattices.

The relative size is defined by the ratio

$$\gamma = \frac{D_B}{D_A} \leq 1 \ . \tag{S29}$$

The size ratio $\gamma = D_B/D_A$ between grafted nanoparticles is used here as a geometric control parameter, following analogies to atomic binary crystals. Our analysis focuses on the regime $0.4 < \gamma < 1.0$, where packing arguments and polymer-mediated interactions guide the formation of distinct cubic lattices such as CsCl, ZnS, diamond, and simple cubic. These structures emerge near stoichiometric compositions and are stabilized without invoking directional interactions.

We note that our treatment does not extend to the highly asymmetric γ regimes explored in Ref. [21], where electrostatic and entropic forces can stabilize FCC-like assemblies of large particles in the presence of smaller counterions. Such mechanisms, while insightful, are beyond the scope of this study.

Our system operates at low added-salt concentration; the effective electrostatic interactions are primarily determined by the surface functional groups and the local ionic environment. While added salt may influence screening and correlation effects, such scenarios are not explored here and warrant further investigation.

The charge will be defined by q_A, q_B and the environmental conditions by the Debye length λ_{DB}. We further Assume that the NPs are at their closest approach allowed by the hard spheres diameter D_A, D_B, i.e. at their maximal packing fraction for the corresponding value of γ and interacting with a Debye-Huckel potential

$$V(r) = \frac{e^2}{4\pi\varepsilon_0} q_A q_B \frac{e^{-\kappa r}}{r} C \quad , r \geq \frac{D_A + D_B}{2} \ , \tag{S30}$$

where the factor C is typically $e^{-\kappa D}/(1+\kappa D)$ where D is the closest distance, but this does not need to be considered here and we will show our results for $C = 1$. The same potential with the appropriate charges are used for $A-A$ and $B-B$ interactions. Here, $\kappa = \frac{1}{\lambda_{DB}}$.

Ref.[18] uses a potential

$$V_{ij}(r) = \frac{e^2}{4\pi\varepsilon_0} \frac{q_i e^{\kappa \frac{D_i}{2}}}{1+\kappa\frac{D_i}{2}} \frac{q_j e^{\kappa \frac{D_j}{2}}}{1+\kappa\frac{D_j}{2}} \frac{e^{-\kappa r}}{r} \quad , r \geq \frac{D_i + D_j}{2} \ , \tag{S31}$$

The same as Eq. S30 if instead of q_i, one uses the renormalized charge $\bar{q}_i = \frac{e^{\kappa \frac{D_i}{2}}}{1+\kappa\frac{D_i}{2}} q_i$. In fact, Ref.[42] provides a rigorous justification for this choice of effective charge in the context of the Dressed Ion Theory (DIT), for the case $D_A = D_B$ ($\gamma = 1$). Full use of Eq. S31 does give slightly different results when compared to Eq. S30, but its consistent use for $\gamma \neq 1$ requires also defining a dielectric function within DIT and the corresponding self consistent values for the Debye length, which needs of major theory developments not readily available, and therefore fall beyond the scope of this paper. We therefore stick to the simpler Eq. S30.

Table S10: Structural and geometrical properties of the lattices.

Lattice	Space Group	Wyckoff positions	γ_c	n_{AB}	c_L	n_{AA}
CsCl	Pm-3m (221)	A-1a B-1b	$\sqrt{3}-1 \approx 0.7321$	8	$\frac{1}{\sqrt{3}} \approx 0.5774$	6
NaCl	Fm-3m (225)	A-4a B-4b	$\sqrt{2}-1 \approx 0.4142$	6	$\frac{1}{\sqrt{2}} \approx 0.7071$	12
ZnS	F-43m (216)	A-4a B-4c	$\sqrt{\frac{3}{2}}-1 \approx 0.2247$	4	$\sqrt{\frac{2}{3}} \approx 0.8165$	12

The main characteristics of the lattices is summarized in Table S10. These three lattices are such that there exists a value of γ_c, such that for $\gamma > \gamma_c$ the A (or B) are in contact with n_{AB} B (or A) NPs, while for $\gamma < \gamma_c$ the A NPS are the ones in contact and either in a fcc structure for both NaCl, ZnS ($n_{AA} = 12$) or a simple cubic for CsCl ($n_{AA} = 6$) with B NPs occupying the interstitial sites. For $\gamma > \gamma_c$, a simple geometric calculation gives the gap between two A NPs as

$$\bar{r}_{AA} = r_{AA} - D_A = (\gamma - \gamma_c) c_L D_A \ , \tag{S32}$$

where $r_{AA} > D_A$ is the nearest neighbor (A-A) distance, which becomes $r_{AA} = D_A$ at $\gamma = \gamma_c$ where the A NPs are in contact. The coefficient c_L is given in Table S10.

The free energy of each lattice is described by the corresponding Madelung constant M defined by

$$E_L(D_A, \gamma, \kappa, q) \equiv \frac{\mathcal{N}_P}{2} \frac{e^2 q^2}{4\pi\varepsilon_0 D_A} e_L(\kappa, \gamma) = \frac{\mathcal{N}_P}{2} \frac{e^2 q^2}{4\pi\varepsilon_0 D_A} \left\{ \begin{array}{ll} \frac{2}{1+\gamma} M_L(\kappa, \gamma) & \gamma > \gamma_c \\ \frac{2}{1+\gamma_c} M_L(\kappa, \gamma_c) & \gamma \leq \gamma_c \end{array} \right. \tag{S33}$$

where $\mathcal{N}_P$ is the number of NPs, D_A is the diameter of the A-NP.

Table S11: Madelung constant and critcial values of instability $\gamma_{u,L}$ for each Superlattices

Lattice	$M_L(0)$	$\gamma_{u,L}$
CsCl	-1.762675	0.7172
NaCl	-1.747565	0.3256
ZnS	-1.638055	-

An important property is that thus defined, $M_L(\kappa = 0, \gamma) = M_L(0)$, independent of γ and is given by the values quoted in standard textbooks, shown in Table S11. The lowest energy Eq. S33 defines the critical values $\gamma_{u,L}$ where each L lattice becomes unstable, which can be given a simple analytical form

$$\begin{aligned} \gamma_{u,CsCl} &= (\gamma_{c,CsCl} + 1) \frac{M_{NaCl}(0)}{M_{CsCl}(0)} - 1 \\ \gamma_{u,NaCl} &= (\gamma_{c,NaCl} + 1) \frac{M_{ZnS}(0)}{M_{NaCl}(0)} - 1 \ , \end{aligned} \tag{S34}$$

shown in Table S11. As expected, the values of $\gamma_{u,L}$ are slightly lower but close to $\gamma_{c,L}$. In fact, on physical grounds one does not need to distinguish between the two and consider $\gamma_{c,L}$ as defining the instability since for $\gamma < \gamma_{c,L}$ the B-particles are allowed to "rattle" within the lattice, but here we will keep the distinction as it makes calculations more consistent.

In Fig. S25 we show the stability of the different lattices for screened interactions ($\kappa > 0$). It is

$$\text{CsCl} \overset{\gamma_{u,CsCl}}{\underset{\gamma_{c,CsCl}}{\approx}} \text{NaCl} \overset{\gamma_{u,NaCl}}{\underset{\gamma_{c,NaCl}}{\approx}} \text{ZnS} \ . \tag{S35}$$

With shorter Debye lengths (lower pH) the ZnS structure is more stable, i.e $\gamma_{u,NaCl}(\kappa)$ is an increasing function with κ.

Inclusion of Short Range Repulsion

The electrostatic contribution has been idealized as consisting of a charge at the center of a hard sphere, or equivalently, a uniformly distributed charge on the surface of their respective NP diameters. In reality the charge is neither uniformly distributed nor entirely located at the exterior of the

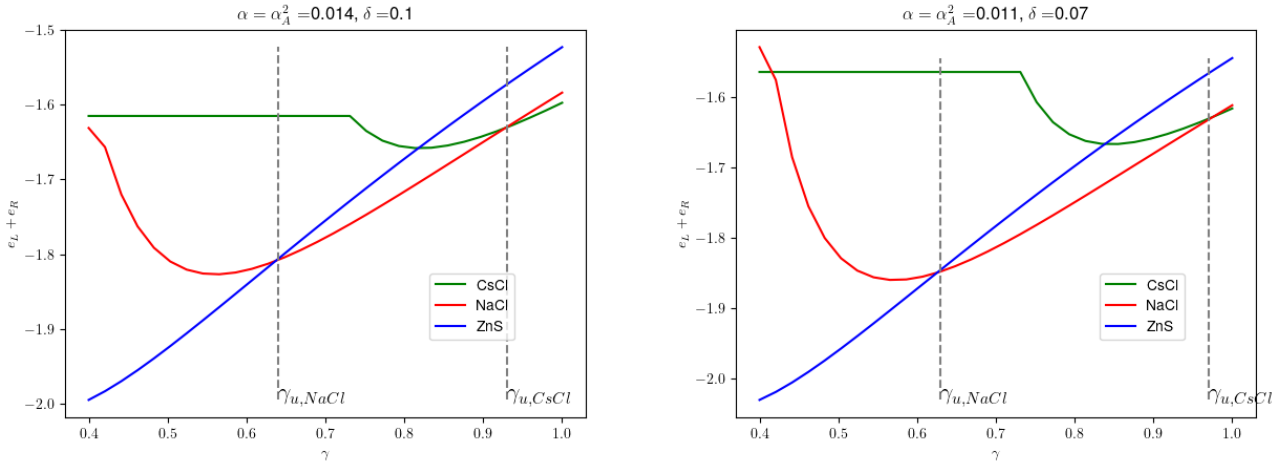

(a) $e_L + e_R$ for $\alpha = 0.014, \delta = 0.1$.

(b) $e_L + e_R$ for $\alpha = 0.011, \delta = 0.07$.

Fig. S26. Energy Eq. S40 incuding the repulsion term.

NP, so we need to consider the role of the discrete charges, which lead to electrostatic correlations. Given that the consideration of a finite Debye length does not modify any of the main conclusions, we will consider the case $\kappa = 0$. We start with the identity

$$\sum_{i\in\mathcal{A}_1}\sum_{j\in\mathcal{A}_2}\frac{q_iq_j}{|\mathbf{r}_i-\mathbf{r}_j|} = \sum_{i\in\mathcal{A}_1}\sum_{j\in\mathcal{A}_2} q_iq_j\left(\frac{1}{|\mathbf{r}_i-\mathbf{r}_j|}-\frac{1}{r_{AA}}\right) + \frac{1}{r_{AA}}\sum_{i\in\mathcal{A}_1}\sum_{j\in\mathcal{A}_2} q_iq_j \ , \tag{S36}$$

where $\mathbf{r}_i$ represent the actual position of the charges. The contribution of the right hand side is the contribution of a uniform surface charge and has already been included in the calculation of the Madelung energy. Therefore, the electrostatic correlation $A-A$ energy for $\gamma > \gamma_c$ is

$$\begin{aligned} U^c_{A-A} &= \frac{e^2}{4\pi\varepsilon_0}\sum_{i\in\mathcal{A}_1}\sum_{j\in\mathcal{A}_2} q_iq_j\left(\frac{1}{|\mathbf{r}_i-\mathbf{r}_j|}-\frac{1}{r_{AA}}\right) = \frac{e^2}{4\pi\varepsilon_0}\sum_{i\in\mathcal{A}_1}\sum_{j\in\mathcal{A}_2} q_iq_j\frac{1}{|\mathbf{r}_i-\mathbf{r}_j|} - \frac{e^2}{4\pi\varepsilon_0}\frac{Q_{\mathcal{A}_1}Q_{\mathcal{A}_2}}{r_{AA}} \\ &\approx \frac{e^2}{4\pi\varepsilon_0}\frac{Q_{\mathcal{A}_1}Q_{\mathcal{A}_2}}{r_c+\bar{r}_{AA}} - \frac{e^2}{4\pi\varepsilon_0}\frac{Q_{\mathcal{A}_1}Q_{\mathcal{A}_2}}{r_{AA}} \equiv \frac{q^2e^2}{4\pi\varepsilon_0 D_A}\frac{\alpha_{\mathcal{A}_1}\alpha_{\mathcal{A}_2}}{\delta + c_L(\gamma-\gamma_c)} - \frac{q^2e^2}{4\pi\varepsilon_0 D_A}\frac{\alpha_{\mathcal{A}_1}\alpha_{\mathcal{A}_2}}{r_{AA}/D_A} \end{aligned} \tag{S37}$$

r_c is a cut-off expected to be of order of 1 nm, defining the closest approach for two charges in different NPs and $Q_{\mathcal{A}_i}$ are the sum of all charges within the region $\mathcal{A}_i$. Therefore the parameter δ is defined

$$\delta = \frac{r_c}{D_A} << 1 \tag{S38}$$

since D_A is of the order of 40 nm. Furthermore $r_{AA}/D_A \approx 1$, which justifies dropping the last term. Also, α the fraction of charge in regions $\mathcal{A}_i$,

$$\alpha_{\mathcal{A}_1} = \frac{Q_{\mathcal{A}_1}}{q} < 1 \tag{S39}$$

In this way, the energy of the lattice becomes

$$E_L = \frac{\mathcal{N}_P}{2}\frac{e^2q^2}{4\pi\varepsilon_0 D_A}\left(e_L(0,\gamma) + \frac{n_{AA}}{2}\frac{\alpha}{\delta + c_L(\gamma-\gamma_c)}\right) \equiv \frac{\mathcal{N}_P}{2}\frac{e^2q^2}{4\pi\varepsilon_0 D_A}\left(e_L(0,\gamma) + e_R(\alpha,\delta,\gamma)\right) \ , \tag{S40}$$

where $\alpha \equiv \alpha_{\mathcal{A}_1}\alpha_{\mathcal{A}_2}$

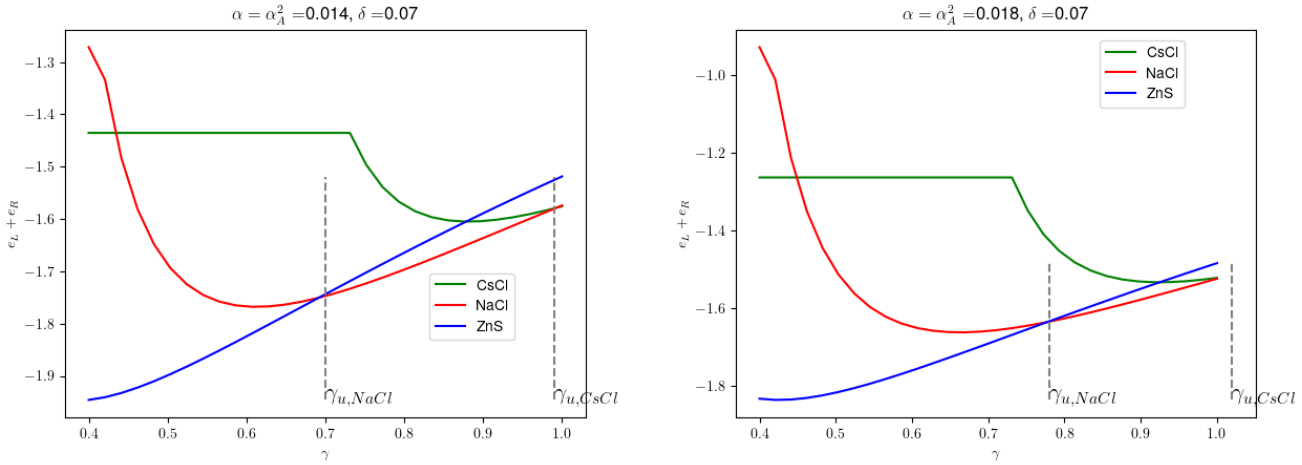

(a) $e_L + e_R$ for $\alpha = 0.014, \delta = 0.07$.

(b) $e_L + e_R$ for $\alpha = 0.018, \delta = 0.07$.

Fig. S27. Energy Eq. S40 incuding the repulsion term. Increasing α shifts $\gamma_{u,L}$ towards higher values.

Fig. S26 shows two representative results where

$$\gamma_{CsCl,u} \approx 0.9 \quad , \quad \gamma_{NaCl,u} \approx 0.65 \tag{S41}$$

which matches the experimental results. The first corresponds to $\alpha = 0.014, \delta = 0.1$, which for D_A= 40 nm corresponds to a cut-off r_c=4 nm, and a fraction $\alpha_{\mathcal{A}} = 0.11$ or 11% of the charge in close contact. The second is $\alpha = 0.011, \delta = 0.07$, which for $D_A = 40$ nm is $r_c = 3$ nm and $\alpha_{\mathcal{A}} = 0.1$ or 10% of the charge in close contact. These numbers are very reasonable and provide a cross-check of the assumptions that have been made.

In the limit $\alpha \to 0$, the correlation term disappears and we recover the ideal case, shown in Fig. S25a. The effect of increasing the charge fraction α for a fixed cut-off, taken as the value in Fig. S26b ($\delta = 0.07$) is shown in Fig. S27. Increasing α makes the A-A repulsion stronger and consequently, shifts $\gamma_{u,L}$ to larger values eventually making CsCl unstable for all values of $\gamma \leq 1$. Further increasing α pushes enhances the stability of the ZnS lattice for broader values of γ.

It could be argued that a similar correlation, but leading to an attraction contribution, exists for the terms $A - B$. Following the same steps as for $A - A$ contributions this would give for $\gamma \geq \gamma_c$

$$e_A(\alpha', \delta') = -n_{AB} \frac{\alpha'}{\delta'} \ , \tag{S42}$$

where δ', α' are the equivalent parameters defined above. Because A,B NPs are in contact for $\gamma > \gamma_c$, the term has no explicit dependence on γ. The complete lattice energy becomes

$$E_L = \frac{\mathcal{N}_P}{2} \frac{e^2 q^2}{4\pi\varepsilon_0 D_A} \left(e_L(0, \gamma) + e_R(\alpha, \delta, \gamma) + e_A(\alpha', \delta') \right) \ . \tag{S43}$$

Now, the energy depends on two additional parameters δ', α'. A reasonable assumption is $\alpha' = \gamma^2 \alpha$, accounting for the smaller solid angle, i.e. the higher curvature, in the $A - B$ region where the charges are close. As for the parameter δ', we will assume $\delta' = l\delta$, with $l > 1$. Fig. S28 shows results with $l = 4$ with the same parameters as Fig. S26(a) yielding similar conclusions, where $\gamma_{u,L}$ values are increased from their ideal values.

The conclusion from the calculations in Fig. S26 and Fig. S28 is that correlations making an $A-A$ repulsion larger in magnitude than $A - B$ attraction (and this is why $l > 1$ is needed in Eq. S43) shifts $\gamma_{u,L}$ towards higher values and away from the ideal case. This effect is already well captured

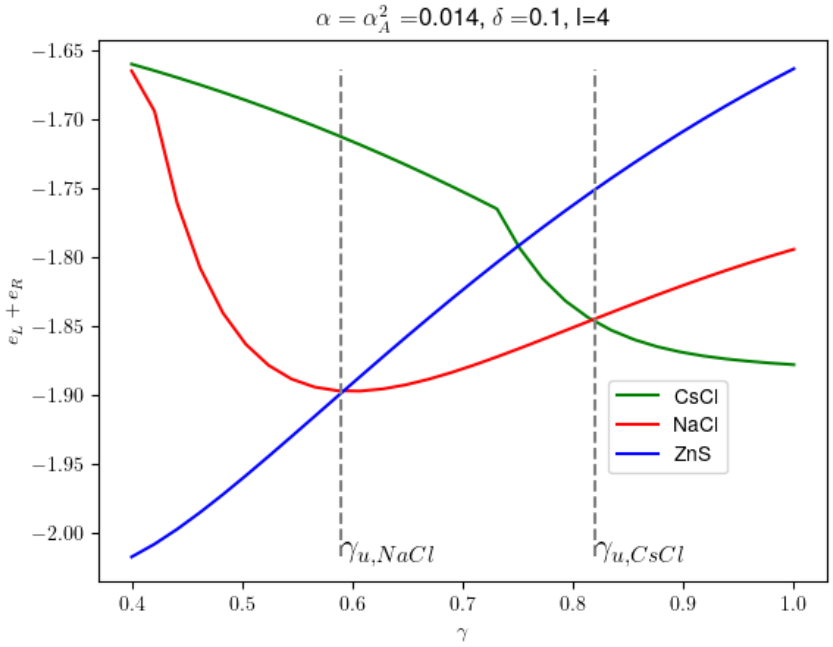

Fig. S28. Energy Eq. S43, including $A-A$ and $A-B$ correlations.

by the simpler model defined by Eq. S40, so at the semi quantitative level of our approach, the more elaborated energy and the additional parameters Eq. S43 are not necessary to consider.

Analysis of ζ-potentials and charging process

Fig. S29 shows the experimental values for the ζ potentials as a function of pH. Those potentials corresponds to isolated NPs, and therefore we will analyze them in the context of the Poisson-Boltzmann equation for a charged sphere.

In dimensionless variables $u = r/\lambda_{DB}$, $\phi = \frac{e\psi}{k_B T}$ where ψ is the electric potential, $\lambda_{DB}^2 = 1/(8\pi l_B I)$ is the Debye length, with $l_B = \frac{e^2}{4\pi\varepsilon_0\epsilon_r}$ the Bjerrum length and $I = 10^{-\min(\text{pH},14-\text{pH})}$ the ionic strength, the PB equation is

$$\frac{1}{u^2}\frac{d}{du}\left(u^2\frac{d\phi(u)}{du}\right) = -\sum_{a=1}\frac{q_a n_a^\infty}{2I}e^{-q_a\phi(u)} = \sinh(\phi(u)) \tag{S44}$$

or

$$\begin{aligned}\frac{d\Psi(u)}{du} &= u^2\sinh(\phi(u))\\ \frac{d\phi(u)}{du} &= \frac{1}{u^2}\Psi(u)\\ \Psi(u) &= -u^2\hat{E}(u)\ ,\end{aligned} \tag{S45}$$

with $\hat{E}(u) = e\lambda_{DB}E(u)/k_BT$, where $E(u)$ is the electric field.

The domain is $R \le r \le L$, where L is the size of the box. In dimensionless variables $u \in$

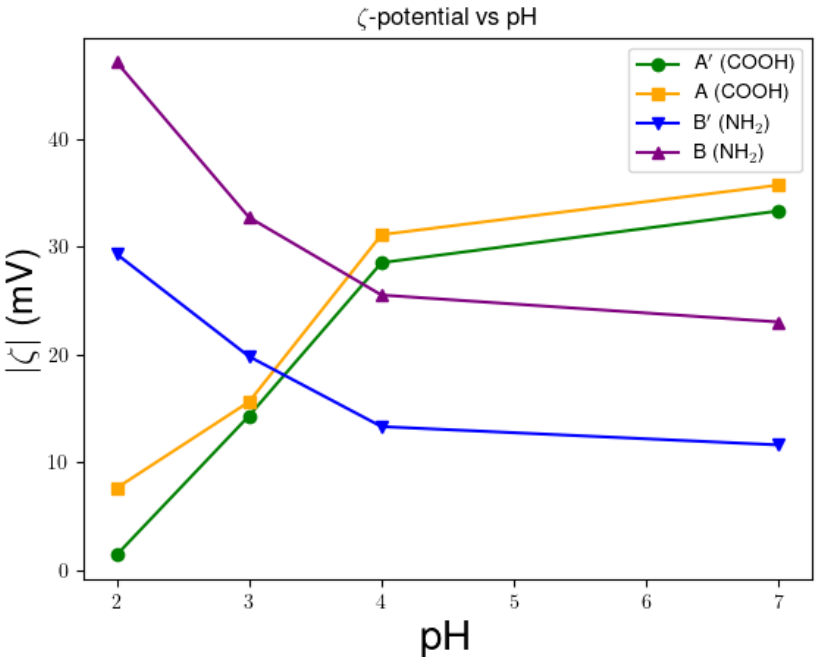

Fig. S29. Experimental ζ-potential as a function of pH. The data is taken from a previous publication Ref. 22.

$[\frac{R}{\lambda_{DB}}, \frac{L}{\lambda_{DB}}] \equiv [\hat{R}, \hat{L}]$ the boundary conditions are

$$\begin{aligned} \hat{E}(\hat{R}) &= 2\ \mathrm{sign}(\sigma)\frac{1}{\hat{\lambda}_{GC}} \rightarrow \Psi(\hat{R}) = -2\ \mathrm{sign}(\sigma)\frac{\hat{R}^2}{\hat{\lambda}_{GC}} \\ \hat{E}(\hat{L}) &= 0 \rightarrow \Psi(\hat{L}) = 0\ , \end{aligned} \tag{S46}$$

where $\hat{\lambda}_{GC} = \frac{\lambda_{GC}}{\lambda_{DB}} = \frac{e}{2\pi l_B \sigma \lambda_{DB}}$ is the dimensionless Guoy-Chapman length.

Eq. S45 with boundary condition Eq. S46 was solved using as initial value the potential $\phi(\hat{R}) = \frac{e\zeta}{k_B T}$ as obtained from the experimental values, with a value for $L = c\lambda_{DB}$, where $c = 6 - 8$, which is equivalent to $\hat{L} \approx \infty$. The charge contained within the NP is obtained from

$$\lambda_{GC} = 2\frac{\lambda_{DB}}{\hat{E}(\hat{R})} \rightarrow Q = 4\pi R^2 \sigma = \frac{4\pi R^2}{2\pi l_B \lambda_{GC}} e = \frac{R^2}{l_B \lambda_{DB}} \hat{E}(\hat{R}) e \tag{S47}$$

The charge Fig. S30 depends on the dielectric constant, implicitly through l_B and λ_{DB}. We will assume the value of the dielectric constant for water $\epsilon_r \approx 78$. The charge also depends on the value of R. The most reasonable choice is half the hydrodynamic radius $R = \frac{D_h}{2}$, yet, the actual value of R corresponds to the radius of the slipping surface (a sphere), which is not theoretically entirely well defined. Therefore, in Fig. S30 we show different choices, which reveals that the actual charge is sensitive to the location of the slipping surface. For the $A'B$ system at pH $= 3 - 4$ gives charges that are approximate balance to 1-1, while for the AB' at pH ≈ 3, the charge of the B' is larger than A.

In general, Fig. S30 is consistent with a pH range $\approx 3 - 4$ where $A'B$ assemble. For pH > 4, the overall charge is too weak to induce attraction, while for $pH < 3$ the charge asymmetry is too large, which in turn induces repulsion.[23] For AB' similar conclusions apply, but the range of pH in which assembly occurs is more narrowly confined to pH ≈ 3.

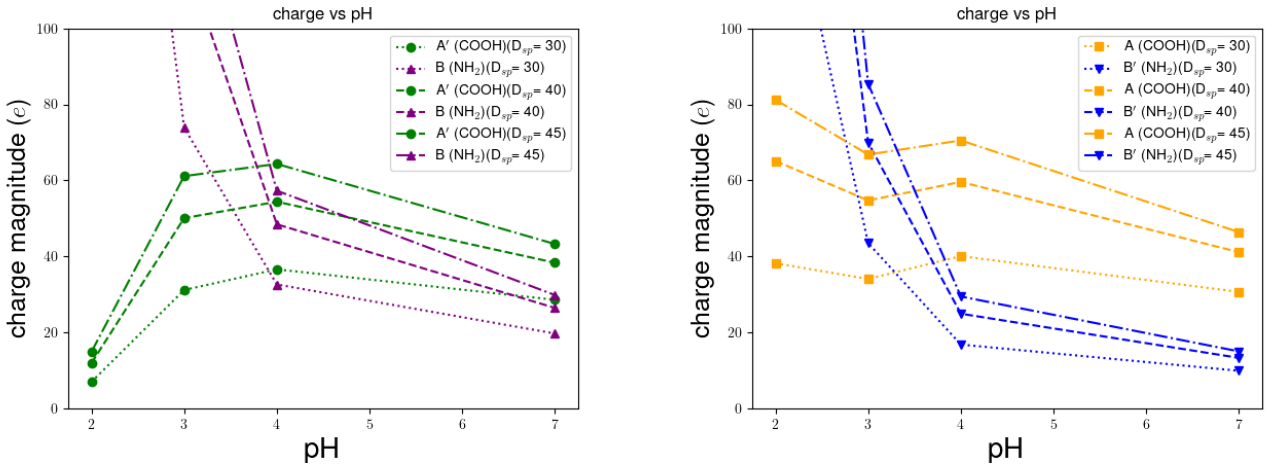

Fig. S30. Charge of the nanoparticle as obtained from Eq. S47. D_{sp} is the location (diameter) of the slipping plane.

The above semi-quantitative estimates do not reveal the origin of the charge. The most straightforward hypothesis is that the charge is entirely determined from the pK$_a$ of the charged species. For a carboxylic group (in water) pK$_a \approx 5$ while for the amine pK$_a \approx 10$. The actual fraction of charged groups is

$$f_0 = \frac{1}{1 + 10^{\pm(\mathrm{pK}_a - \mathrm{pH})} e^{\mp\phi(\hat{R})}} \tag{S48}$$

where $\pm$ refers to carboxylic/amine. The charge is $Q = Q_{max} f_0$, where Q_{max} is the maximum charge, which is obtained when all groups are charged.

Fig. S31 shows Eq. S48 assuming that at pH=7 the potential (and charge) correspond to the experimental value. Using again different values for the slipping surface, the main conclusion is that Eq. S48 fails to describe the charging process. For the COOH groups, Eq. S48 is qualitatively correct in that it predicts that the ζ-potential decreases with pH, but the experimental values show a much slower decay. For the NH_2 groups, Eq. S48 also predicts a decay of the ζ-potential, this is because at this low pH the amine groups are already completely charged and the decay reflects the reduction of ζ with the increased screening of the electrostatic interactions. Yet, the experimental results are consistent with partially charged groups, whose charge is increasing with lowering of the pH. Even if the value of the pK$_a$ is left as a free parameter, the results are not satisfactory. Overall, the picture that emerges from the ζ-potentials is that the charging process is inconsistent by a simple pK$_a$ value as given by Eq. S48.

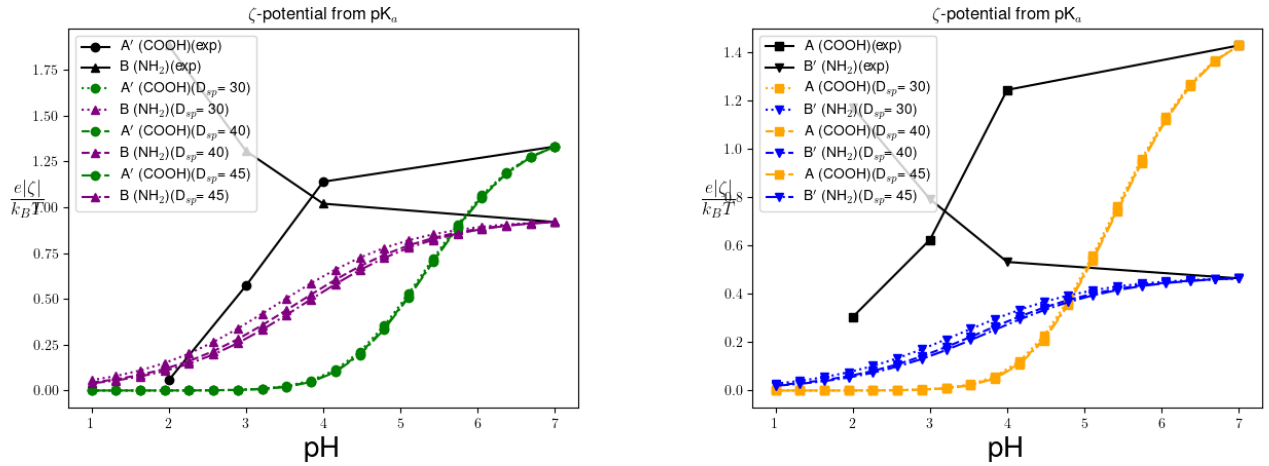

Fig. S31. ζ-potential by assuming a single pK$_a = 5, 10$ for COOH and NH_2 as described in the text. D_{sp} is the location (diameter) of the slipping plane.

A good agreement with the ζ-potential is obtained if one assumes two populations each one with a pK_a. Fig. S32 shows results where the two pK_a for the COOH are (0,20) and for NH_2 (2.05, 10) with the first pK_a population being 99%. The results describe the experimental values, but of course, the actual pK_a values do not lend to an obvious physical interpretation. We believe that the underlying reason is that the polymer and the ions create an environment with a complicated dielectric function. An analysis of this point and the prediction of the NP charge from theory is beyond the scope of this paper and, furthermore, is also not really necessary for the purposes of this paper; We can identify the pH where assembly occurs from the ζ potentials alone, without an actual model to predict the charging process.

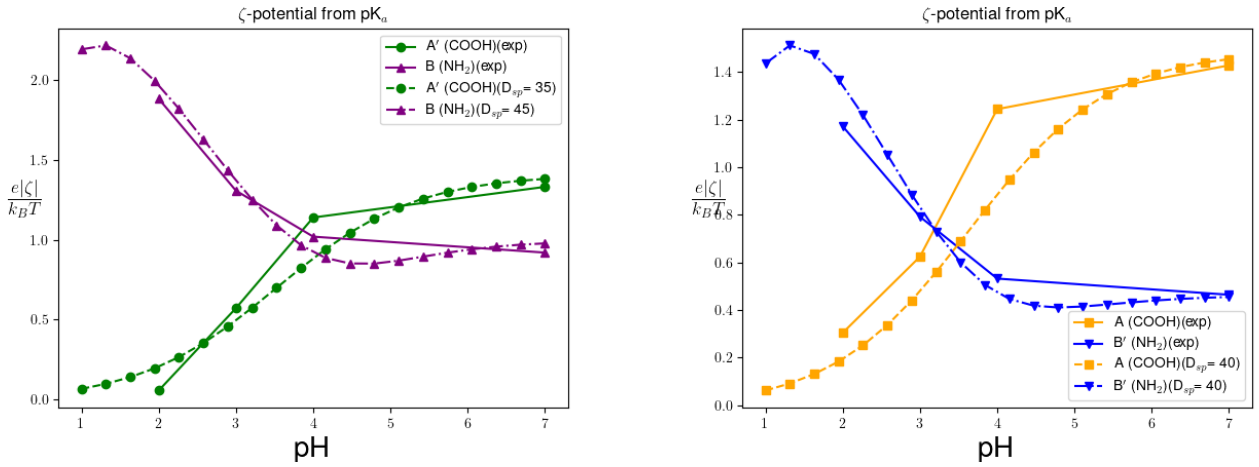

Fig. S32. ζ-potential by assuming two populations with two pK_a values. The experimental and calculated ζ-potential is overlaid to show a match.

All atom molecular-dynamics simulations

The electrolytes in the experimental system are HCl, and regulate the charge. Here, we consider the simpler NaCl electrolyte instead. We further assume completely charged COO^- and NH_3^+ groups. Although these approximations do modify significant aspects of the system as compared to the experiment, they capture the essential physics: the competitive binding of counterions with respect to end-polymer groups, so they enable to establish the role of atomistic or molecular interactions in the assembly process. The fundamental question we aim to address is the nature of electrostatic correlations and whether oppositely end-polymer charged-group attraction is prevalent over counterion binding and the strength of the same end-polymer charged groups against electrolyte screening, which is essential, as discussed, in expanding the stability of open superlattices.

To gain insight into the interplay of repulsive and attractive interactions between oppositely charged, polymer-grafted NPs, we conducted simplified numerical simulations using planar geometries. While this approximation does not capture the full curvature of spherical NPs, it enables a tractable exploration of key trends in electrostatic potentials and overlap energies: namely, the role of hydrogen bonds, the strength of the COO-NH_3^+ coupling, and the presence of electrostatic correlations. These simulations are not intended to quantitatively reproduce experimental structures, but rather to support our theoretical framework and rationalize how competing interactions can stabilize a range of cubic superstructures. Given the current computational limitations, particularly for realistic NPs sizes and grafting densities, more detailed simulations remain a challenge for future work.

We consider two walls with grafted PEG, see Fig. S33 terminated with either COO^- or NH_3^+. In some cases, regular PEG, terminated with CH_3, was used as a control. The walls are periodic

along the perpendicular direction with wall-to-wall distance D_w. They provide an approximation on how facets of the nanoparticle core with grafted PEG-terminated groups interact with each other. Water is included within the SPC/E model. Despite its simplifications, the model describes the experimental system on short space (and time) scales. For example, binding of Na^+ (and Cl^-) to COO^- (and NH_3^+) neutralizes each individual charge and is therefore equivalent to binding (or releasing) hydronium H_3O^+. Therefore, the model captures the essential aspects of the real system.

We investigated the two walls grafted as follows, see Fig. S33:

(a) COO^--NH_3^+

(b) NH_3^+-NH_3^+

(c) COO^--COO^-

Cases (a) investigates opposite charge attraction, while (b),(c) equal charge repulsion. Since simulations include electrolytes, we aim to assess the role of general electrostatic correlations, including hydrogen bonding, in opposite group attraction and repulsion. The main result is provided in Fig. 4 (c), which illustrates the strong COO^--NH_3^+ binding and equal charge repulsion. Fig. 4(d), see also the more complete Fig. S33, shows simulation snapshots where the water molecules have been removed for clarity. For oppositely terminated end-groups, Fig. S33 (a,d) shows very significant binding of COO^--NH_3^+ groups (roughly 1/3 of them, favored by hydrogen bonds, see Fig. 4(c)) as well as neutralization of the charge by counterions, akin to COO^--H^+ and NH_3^+-OH^- binding. The main conclusion is that even at very high electrolyte concentration of 0.5m, attraction persists. Fig. S33 (b,c) and (e,f) provide snapshots from same groups. Here, the large amount of electrolytes do not screen the repulsion between same end-terminated groups, thus providing clear evidence on the role of repulsions.

In order to provide a quantitative characterization, we introduce the following quantities

$$f_{\mathrm{COO^-}}(z) = \frac{N_{\mathrm{COO^-}}(z)}{N_{\mathrm{Total\,COO^-}}} \qquad \text{(S49)} \qquad f_{\mathrm{NH_3^+}}(z) = \frac{N_{\mathrm{NH_3^+}}(z)}{N_{\mathrm{Total\,NH_3^+}}} \qquad \text{(S50)}$$

$$f_{\mathrm{PEG_{COO^-}}}(z) = \frac{PEG_{COO^-}(z)}{PEG_{COO^-} + PEG_{NH_3^+}} \qquad \text{(S51)} \qquad f_{\mathrm{PEG_{NH_3^+}}}(z) = \frac{PEG_{NH_3^+}(z)}{PEG_{COO^-} + PEG_{NH_3^+}} \qquad \text{(S52)}$$

$$f_{\mathrm{Na^+}}(z) = \frac{N_{\mathrm{Na^+}}(z)}{N_{\mathrm{Total\,Na^+}}} \qquad \text{(S53)} \qquad f_{\mathrm{Cl^-}}(z) = \frac{N_{\mathrm{Cl^-}}(z)}{N_{\mathrm{Total\,Cl^-}}} \qquad \text{(S54)}$$

where $N_{COO^-}(z)$ and $N_{NH_3^+}(z)$ are the numbers of COO^- and NH_3^+ end groups at coordinate z, and $N_{\mathrm{Total\,COO^-}}$ and $N_{\mathrm{Total\,NH_3^+}}$ are the total numbers of these end groups in the system, with same definitions for $N_{Na^+}(z)$ and $N_{Cl^-}(z)$ and $N_{\mathrm{Total\,Na^+}}$ and $N_{\mathrm{Total\,Cl^-}}$ are their total numbers in the system.

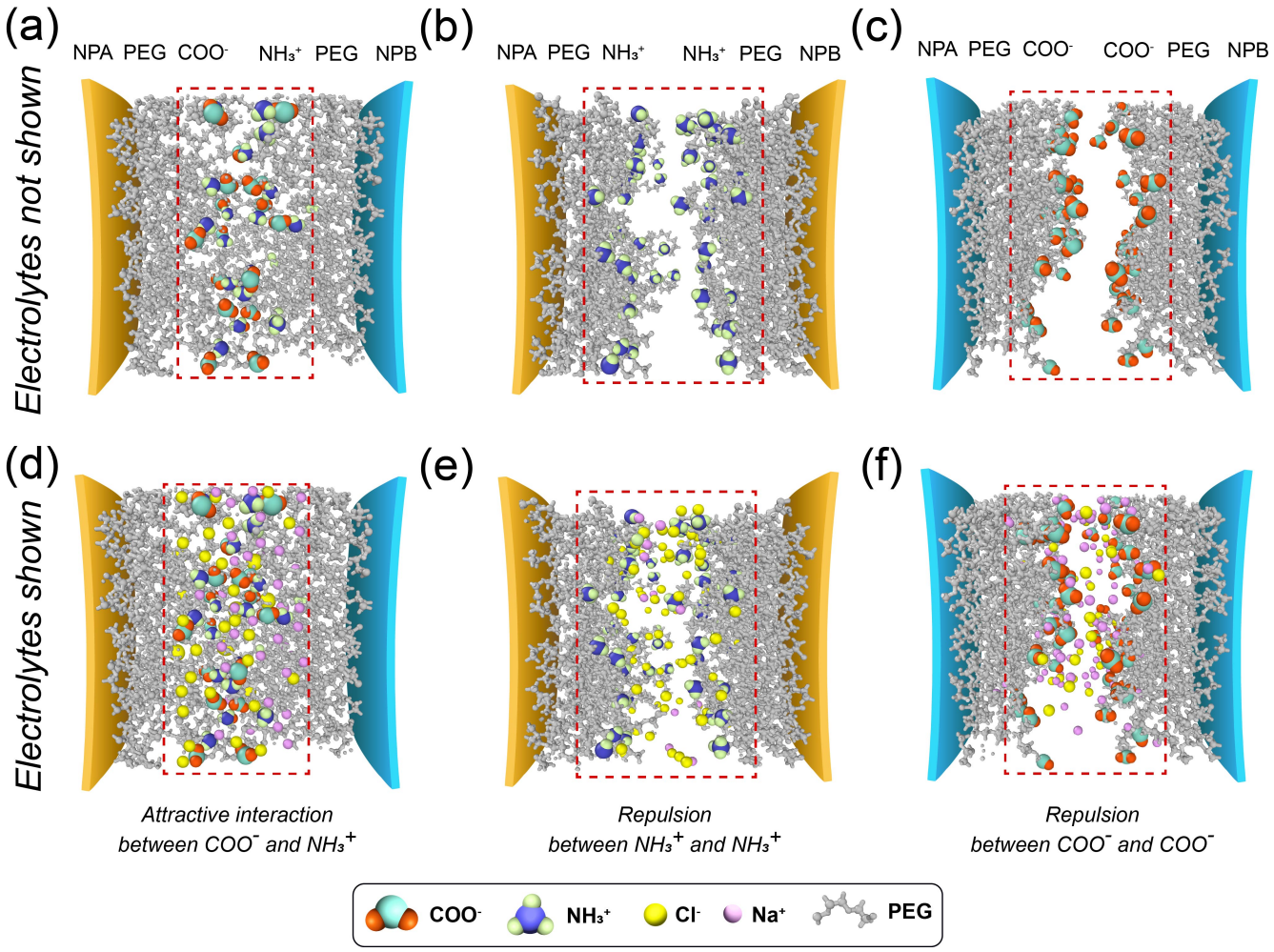

Fig. S33. Snapshots illustrating the attractive interaction and repulsion among charged end groups. The top row has water and electrolytes removed, while the bottom includes electrolytes also.

Fig. S34 shows these fractions for the wall at a large $D_w \approx 10$ nm separation. Basically, the terminated groups are enclosed within the PEG chains and are neutralized by significant binding and a subsequent diffuse layer of counterions, see Fig. S34 (b). Also shown in Fig. S34 (b) is the maximum of the end group distribution, showing that this maximum matches the maximum of the counterion distribution.

Fig. S35 shows the same system but at a much closer separation $D_w \approx 4$ nm. Here, the terminated end groups significantly stretch to form COO^--NH_3^+ pair, pushing the electrolytes within the ligands, as shown in Fig. S35 (b) where the maximum of the counterion is now displaced from the maximum of the end-groups, thus illustrating the strong COO^--NH_3^+ correlations. Overall, the simulations support the assumptions made in the effective model where: a) There is strong COO^--NH_3^+ attractive correlations b) Strong same charge repulsion, which is not screened by electrolytes c) Electrolytes are expelled for maximum attraction. A more elaborated description of the simulations and its implications will be provided in a subsequent publication.

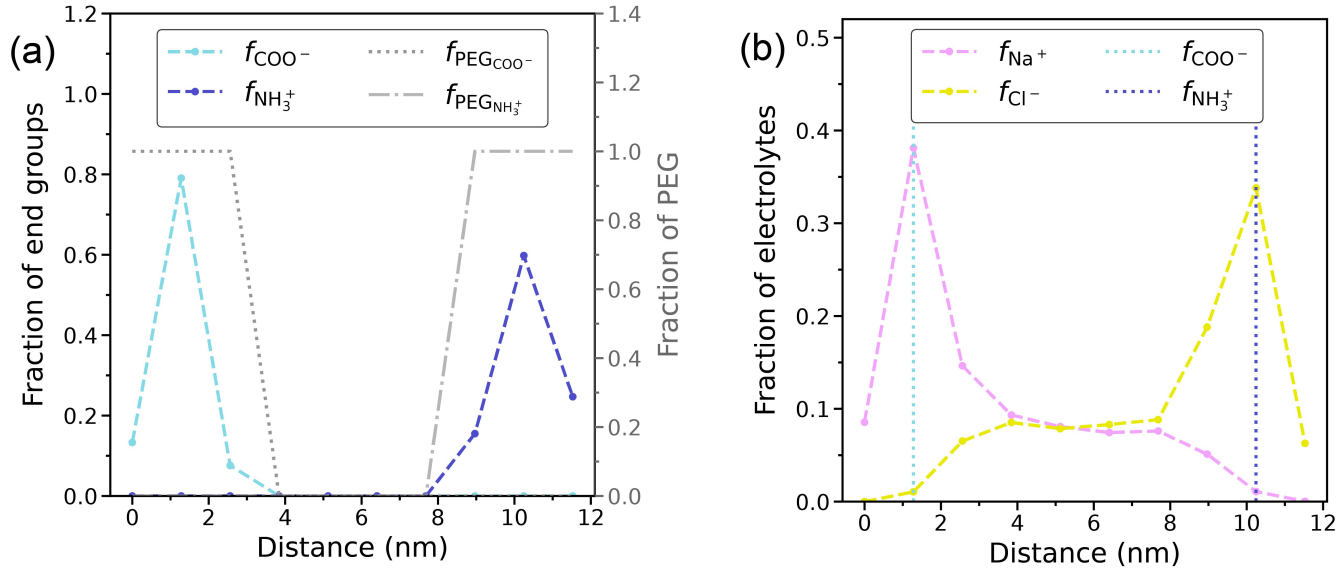

Fig. S34. Distributions at $D_w = 11.7$ nm for the (a) charged end groups and polymer and (b) electrolytes. In (b) the separation distance where f_{COO^-} and $f_{NH_3^+}$ are a maximum are shown with dotted lines.

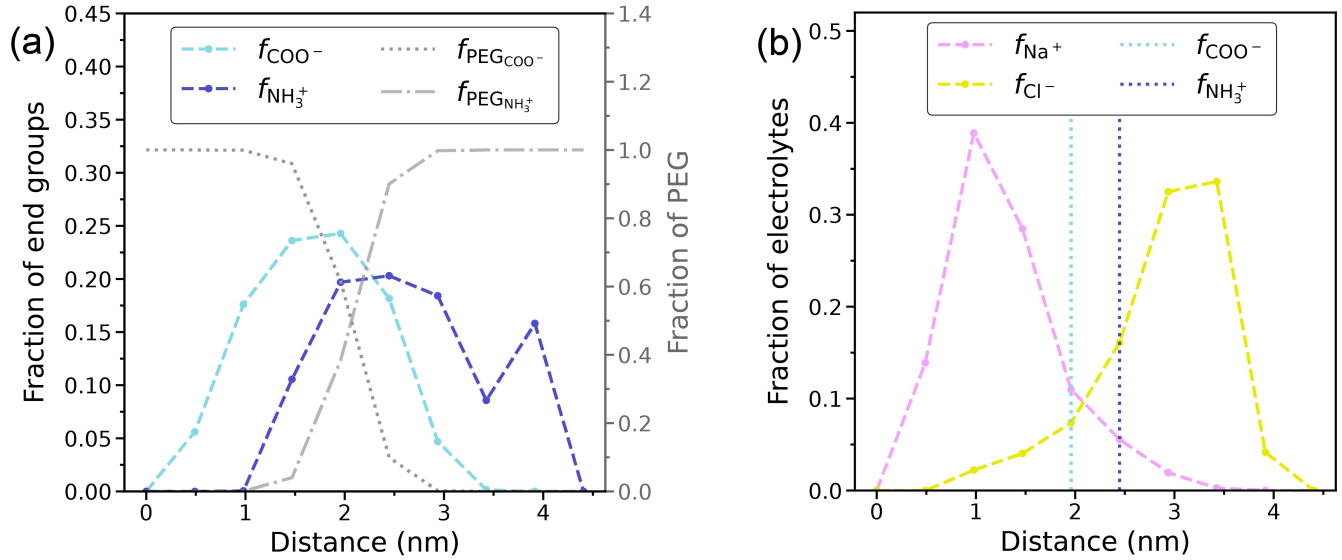

Fig. S35. Distributions at $D_w = 4.6$ nm for the (a) charged end groups and polymer and (b) electrolytes. In (b) the separation distance where f_{COO^-} and $f_{\mathrm{NH}_3^+}$ are a maximum are shown with dotted lines.